International Journal of Earth Sciences (2021) 110:2923–2953
https://doi.org/10.1007/s00531-021-02092-y

ORIGINAL PAPER

Two-phase late Paleozoic magmatism (~ 313–312 and ~ 299–298 Ma) in the Lusatian Block and its relation to large scale NW striking fault zones: evidence from zircon U–Pb CA–ID–TIMS geochronology, bulk rock- and zircon chemistry

A. Käßner[1] · M. Tichomirowa[1] · M. Lapp[2] · D. Leonhardt[2] · M. Whitehouse[3] · A. Gerdes[4]

Received: 25 February 2021 / Accepted: 7 July 2021 / Published online: 12 August 2021

Abstract

Late Paleozoic (Variscan) magmatism is widespread in Central Europe. The Lusatian Block is located in the NE Bohemian Massif and it is part of the Saxothuringian Zone of the Variscan orogen. It is bordered by two major NW-trending shear zones, the Intra-Sudetic Fault Zone towards NE and the Elbe Fault Zone towards SW. The scarce Variscan igneous rocks of the Lusatian Block are situated close to these faults. We investigated 19 samples from Variscan plutonic and volcanic rocks of the Lusatian Block, considering all petrological varieties (biotite-bearing granites from the Koenigshain and Stolpen plutons, amphibole-bearing granites from three boreholes, several volcanic dykes, and two volcanites from the intramontane Weissig basin). We applied whole-rock geochemistry (18 samples) and zircon evaporation dating (19 samples). From the evaporation data, we selected six representative samples for additional zircon SHRIMP and CA–ID–TIMS dating. For the Koenigshain pluton, possible protoliths were identified using whole-rock Nd-isotopes, and zircon Hf- and O-isotopes. The new age data allow a subdivision of Variscan igneous rocks in the Lusatian Block into two distinct magmatic episodes. The spatial relation of the two age groups to either the Elbe Fault Zone (298–299 Ma) or the Intra-Sudetic Fault Zone (312–313 Ma) together with reports on the fault-bound character of the dated intrusions suggests an interpretation as two major post-collisional faulting episodes. This assumption of two distinct magmatic periods is confirmed by a compilation of recently published zircon U–Pb CA–ID–TIMS data on further Variscan igneous rocks from the Saxothuringian Zone. New geochemical data allow us to exclude a dominant sedimentary protolith for the Koenigshain pluton as supposed by previous investigations. This conclusion is mainly based on new O- and Hf-isotope data on zircon and the scarcity of inherited zircons. Instead, acid or intermediate igneous rocks are supposed as the main source for these I-type granitoids from the Koenigshain pluton.

Keywords Geochronology · Zircon · Variscan granites · Lusatian block

Introduction

In the Palaeozoic, the closure of the Rheic Ocean and the amalgamation of the supercontinent Pangaea caused the Variscan orogeny in North America, Europe and Asia. In the Bohemian Massif, located in the easternmost part of the European Variscides, the orogen is subdivided into a series of orogenic zones by subordinate subduction zones (Fig. 1, e.g. McCann 2008). Subduction processes at ca. 340 Ma marked the peak metamorphism and the end of plate convergence in the Saxothuringian Zone of Central Europe (Fig. 1, e.g., Schmädicke et al. 1995; Kröner and Willner 1998; Tichomirowa et al. 2005). During the post-collisional period, transpressional and transtensional tectonics resulted

✉ A. Käßner
alexandra.kaessner@mineral.tu-freiberg.de

[1] Institut Für Mineralogie, TU Bergakademie Freiberg, Brennhausgasse 14, 09599 Freiberg/Sachsen, Germany

[2] Saxonian Geological Survey, Halsbrücker Str. 31a, 09599 Freiberg, Germany

[3] Swedish Museum of Natural History, Box 50007, 1045 Stockholm, Sweden

[4] Institut Für Geowissenschaften, Goethe Universität Frankfurt, Altenhoeferallee 1, 60438 Frankfurt am Main, Germany

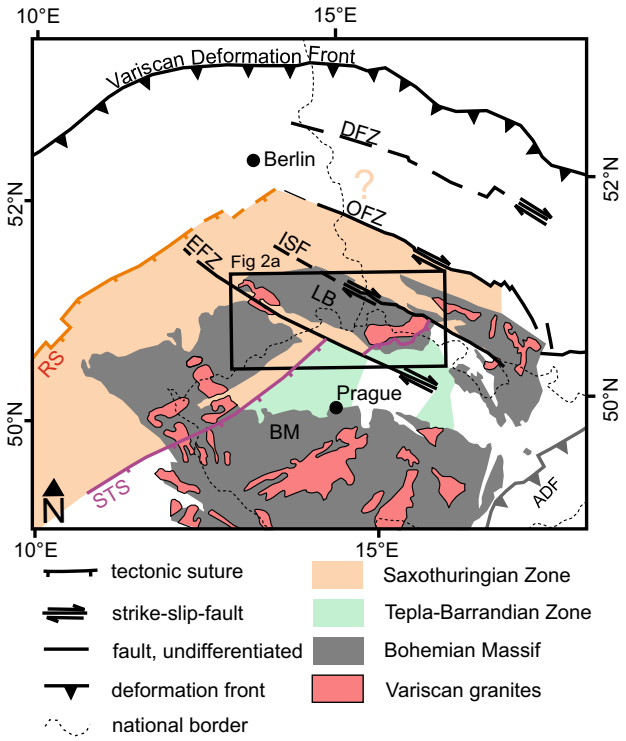

Fig. 1 Simplified Variscan tectonic map of Central Europe after Mazur et al. (2020). *RS* Rhenohercynian Suture, *STS* Saxothuringian Suture, *LB* Lusatian Block, *EFZ* Elbe Fault Zone, *ISF* Intra-Sudetic Fault Zone, *OFZ* Odra Fault Zone, *DFZ* Dolsk Fault Zone, *ADF* Alpine Deformation Front

in significant strike-slip displacement along continental scale NW-trending strike-slip faults, that cut and offset the original EW-trending Variscan zones of the Bohemian Massif (e.g., the Saxothuringian and the Tepla-Barrandean Zones, Fig. 1) in the easternmost part of the European Variscides (e.g. Mazur et al. 2020). Recent tectonic models emphasize a repeated reactivation of these structures under different tectonic stress fields (Edel et al. 2018).

Late Paleozoic late- to post-Variscan igneous rocks (combined here under the term Variscan) of the Bohemian Massif are in many cases bound to strike-slip faults (Oberc-Dziedzic et al. 2015) and their radiometric dating may give information about the temporal evolution of the tectonic activity on these structures. Most of the Variscan igneous rocks have been dated repeatedly by different geochronological methods (summarized by, e.g., Förster and Romer 2010; von Seckendorff 2012) and extensively analysed geochemically (e.g., Hammer 1996; Förster et al. 1999; Hammer et al. 1999; Słaby and Martin 2008; Tichomirowa et al. 2019b). Recently, first high-precision zircon U–Pb CA–ID–TIMS data of Variscan granitic rocks allow to reliably differentiate single magmatic pulses of the post-Variscan period indicating distinct short (1–2 Myr) magmatic periods (Kryza et al. 2014a; Tichomirowa et al. 2019a).

The Lusatian Block, the Jizera mountains and the Karkonosze pluton are part of the Saxothuringian Zone of the NE Bohemian Massif (Fig. 1) and constitute a NW-striking terrane that is bound by two major NW striking fault zones, the Elbe Fault Zone (EFZ) and the Intra-Sudetic Fault Zone (ISF; Figs. 1, 2). Towards the north, the ISF splits into the Inner Lusatian and the Main Lusatian Fault (Fig. 2a). The northernmost constituent of the Lusatian-Jizera-Karkonosze Block is the Lusatian Block, which is bound towards NW by the Cambrian sediments of the Torgau-Doberlug syncline (Geyer et al. 2014). Towards SE, The Lusatian Block is confined by the ESE striking normal faults of the Eger Graben (the prolongation of the Krušné Hory Fault towards E, Fig. 2) against the Early Paleozoic igneous rocks of the Jizera mountains, which are intruded by the granitic Variscan Karkonosze pluton (Fig. 2, Kozdrój et al. 2001).

In the Lusatian Block, the late- to post-Variscan granitoids are subordinate and Variscan volcanic rocks are scarce (Fig. 2). Variscan magmatic activity manifested near the NW striking border faults of the Lusatian Block as granitic plutons, volcanic rocks, and mainly fault-parallel volcanic dykes. These rocks are geochemically and petrologically highly diverse (e.g., Hammer et al. 1999). A relationship between strike-slip-faulting and magmatic activity seems plausible. To understand the tectono-magmatic evolution of the Lusatian Block and its NW striking boundary faults, it is necessary to define precise ages of the fault-bound granitoids. Sources of these rocks need to be understood to interpret the interrelation of faulting and magmatism.

In this study, we present new whole-rock geochemistry and isotope data (Nd- for whole rocks, Hf- and O-isotopes for zircon) of Variscan granitic and rhyolitic-dacitic rocks of the Lusatian Block to infer on sources of these rocks. To determine ages for the igneous rocks, we first applied zircon evaporation dating (Kober et al. 1987) on 19 different Variscan igneous rocks of the Lusatian Block. Based on these data, we chose one sample for zircon U–Pb SHRIMP and six representative samples for high-precision CA-ID-TIMS dating.

Geological setting

Geological setting of the Lusatian Block

The basement of the Lusatian Block is characterized by monotonous flysch-like Precambrian greywacke and pelite sequences (Kröner et al. 1994; Linnemann et al. 2010) that are mainly located in the northern part (Fig. 2a). These sediments were consolidated during the Cadomian orogeny (ca. 570–540 Ma, e.g., Linnemann et al. 2000; Kroner et al. 2007; Linnemann et al. 2010) and intruded by granodioritic plutons at ca. 540–530 Ma (Fig. 2a;

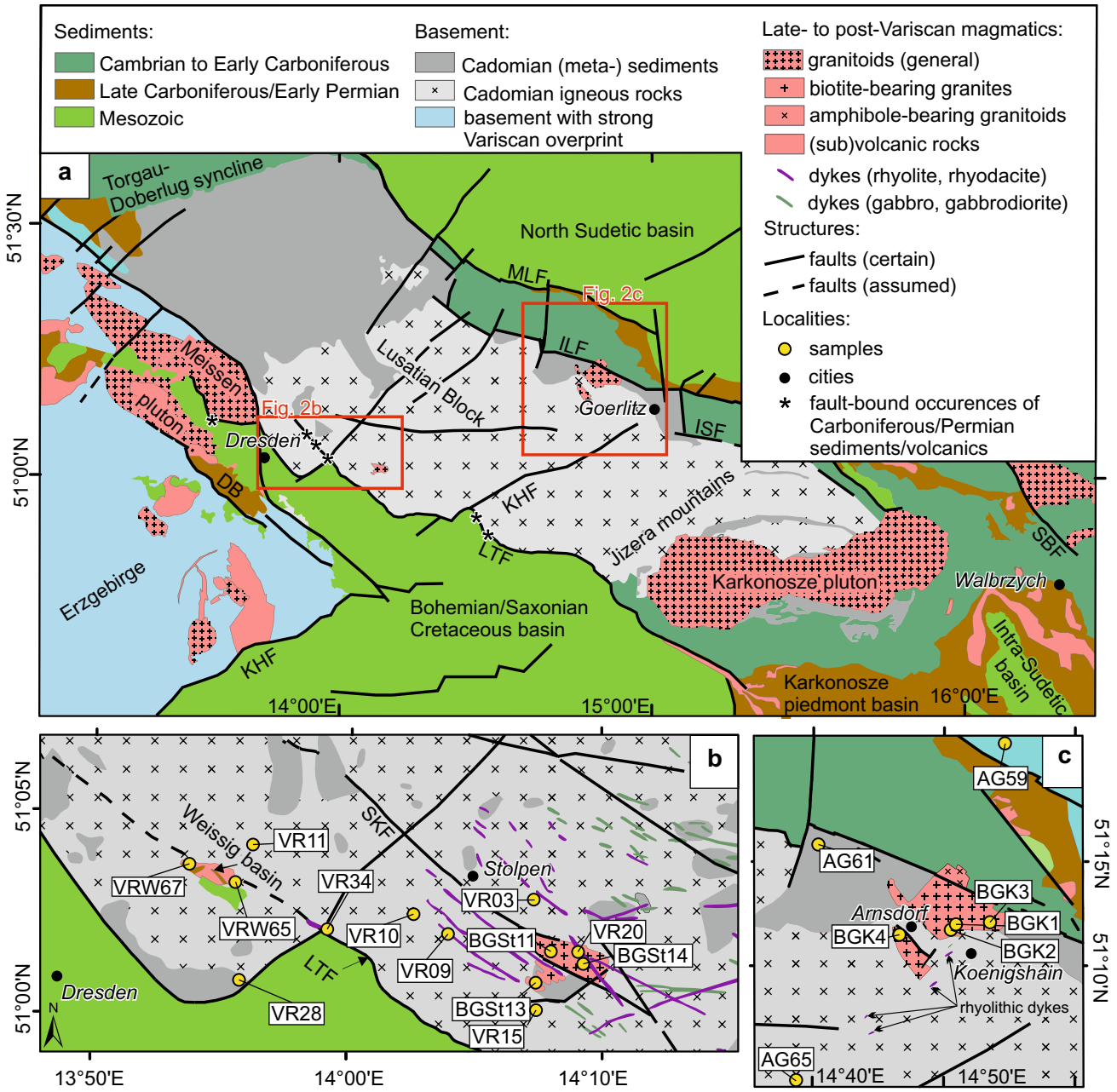

Fig. 2 Geological maps (based on Kozdrój et al. (2001): (**a**) geological map of the Lusatian (-Jizera-Karkonosze) Block with major structures. **b** sample locations of the Stolpen pluton, volcanic dykes, and the volcano-sedimentary Weissig basin, **c** sample locations of amphibole-bearing granitoids and of the biotite-bearing granites of the Koenigshain pluton (Cenozoic sediments and volcanic rocks removed). Abbreviations in a-d are: *LTF* Lusatian Thrust Fault, *SKF* Stolpen-Klotzsche Fault, *ISF* Intra-Sudetic Fault, *ILF* Inner Lusatian Fault, *MLF* Main Lusatian Fault, *SBF* Sudetic Boundary Fault, *KHF* Krušné Hory Fault, *DB* Doehlen basin

Linnemann et al. 2000; Linnemann 2007; Tichomirowa et al. 2001; Tichomirowa 2002) that are mainly located in the southern part of the Lusatian Block (Fig. 2a). The high-grade Variscan metamorphic overprint that characterizes the basement of the adjacent Erzgebirge (Fig. 2a) only affected the rocks of the Lusatian Block along major tectonic lineaments.

During various magmatic events, the Cadomian basement of the Lusatian Block was penetrated by pre-Variscan alkaline basaltic and gabbroic dyke swarms (ca. 400 Ma; Kramer 1977; Kindermann et al. 2003; Abdelfadil et al. 2013; Fig. 2), late Variscan calc-alkaline lamprophyres (330–340 Ma, Abdelfadil et al. 2013), post-Variscan

compositionally diverse felsic igneous rocks (290–340 Ma, e.g., Hammer et al. 1999; Förster et al. 2012; Kryza et al. 2014a), and, subordinately, Mesozoic lamprophyric dykes (ca. 230 Ma, Kramer et al. 1977).

Roughly simultaneously with the post-Variscan magmatism, beginning post-orogenic denudation and contemporaneous deformation of the Variscan mountains led to the formation of intramontane Late Carboniferous/Early Permian molasse basins in the Saxothuringian Zone. Since the basins were uplifted and largely eroded together with the orogen, most of the present intramontane basins represent erosional remnants (Schneider and Romer 2010). Several such basins surround the Lusatian Block, namely the North Sudetic basin, the Intrasudetic basin, the Karkonosze piedmont basin, and the Doehlen basin (Fig. 2a). The Lusatian Block itself is free of molasse sediments, except for the 2.7 km long and 1 km wide Weissig basin, which is located in the prolongation of the Lusatian Thrust Fault of the EFZ (Fig. 2b). The basin fill of the Weissig basin comprises ca. 350 m of interlayered sediments and volcanic rocks. Altogether, ca. 150 m of the basin fill consists of crystal-rich intermediate lava and crystal tuff (Reichel 2012). The stratigraphic sequence of the Weissig basin is subdivided into two formations, namely the Hutberg Formation that predominates in the northwestern part of the basin and the Napoleonstein Formation that predominates in the southeastern part (Reichel 2012). Further dismembered blocks of Permian volcanic and sedimentary rocks (Radebeul, Rossendorf, Rosinendörfchen, Vlči hora, Hodkovice nad Mohelkou; Reichel 2012; Huhle and Lange 2010; Fig. 2a) appear along the Lusatian Thrust Fault.

Variscan magmatism in the Lusatian Block

Variscan plutons are encountered in the entire Bohemian Massif (Fig. 1, Cháb et al. 2007). In the Lusatian-Jizera-Karkonosze Block, the largest of these plutons is the ca. 70 km long and > 20 km wide Karkonosze Pluton, while smaller plutons occur in the northern part (Koenigshain and Stolpen plutons; Fig. 2a–c).

The Karkonosze composite pluton was studied in detail by several authors. Based on whole-rock geochemistry and petrologic evidence, the various lithologies of the Karkonosze composite pluton have been interpreted as the product of mixing of a peraluminous crustal magma with a mafic magma (Słaby and Martin 2008). Epsilon Nd data vary from -7 to -1 and are specific for single rock types of the pluton. These data were interpreted as mixing between two endmembers: (i) an enriched mantle source and (ii) a granitic crustal source (Słaby and Martin 2005). The concept of mixing is supported by the existence of mafic magmatic enclaves and syn-plutonic dykes (Barbarin 2005). The existence of chemically zoned feldspar-phenocrysts and chemical modelling indicates that fractional crystallization also took place during the evolution of the Karkonosze granite (Słaby and Götze 2004). Several attempts have been made to determine the intrusion age and sequence of the various rock types of the Karkonosze pluton using different methods and minerals (e.g., Duthou et al. 1991; Kröner et al. 1994; Kusiak et al. 2009). They thereby observed large scatter in intrusion ages (290–340 Ma) contradicts recent high-precision zircon U–Pb CA-ID-TIMS data that display ages between 312.5 ± 0.3 and 312.3 ± 0.3 Ma for the two main granite facies (Kryza et al. 2014b).

Smaller plutons as well as other subsurface granites were studied in less detail. Petrologically, these rocks were subdivided into amphibole- and biotite-bearing intrusions (Fig. 2b, c, Hammer 1999). The monzogranite of Wiesa, the granodiorite (tonalite) of Kleinschweidnitz (Eidam et al. 1995; Hammer 1996), and a granodiorite encountered in a borehole northeast of Arnsdorf (borehole "Ober Prauske", Hammer 1996) represent amphibole-bearing granitoids. The most prominent of the biotite (± muscovite-)-bearing intrusions is the massif of Koenigshain/Arnsdorf (Fig. 2c), which is composed of three textural varieties: equigranular leucogranite, porphyritic granite, and fine-grained monzogranite (Eidam and Götze 1991; Hecht et al. 1999). The biotite-bearing rocks also include the monzogranites of Stolpen (Hammer 1996). The slightly NW elongated shape and the spatial proximity of the Stolpen pluton to the Stolpen-Klotzsche Fault (Fig. 2b, parallel to the EFZ) support the assumption that the magma intruded along this fault (Kozdrój et al. 2001; Lisowiec et al. 2014). The Koenigshain pluton is bound to the Inner Lusatian Fault (Fig. 2c) and provides petrologic evidence for a relationship between faulting activity and magma intrusion (Hammer 1996; Thomas and Davidson 2016).

Magma sources of the granitoid rocks have been proposed based on whole-rock geochemistry and Sr-, Nd-, O-, and H-isotopic data (Hammer 1996). According to these data, the amphibole- and biotite-bearing granites had different sources. Hammer (1996) interpreted the amphibole-bearing granites as melts formed from mafic amphibolite-facies rocks of the lower crust. Distinctly, the biotite-bearing granites are suggested to be water-undersaturated partial melts from metatonalitic or metapelitic protoliths (Hammer 1996). The composition of altered domains and the mineralogy of secondary accessories indicate a local influence of post-magmatic fluids to the Stolpen biotite-bearing granite. Enrichment in some HFSE and LILE (Th, U, Y, Hf, Nb, and Ta) and a high halide content (fluorite) of altered domains indicate a mantle origin of these fluids (Lisowiec et al. 2013). Different minerals and methods have been used to determine the intrusion age of the granitoid rocks of both the Koenigshain pluton and the Stolpen pluton (Fig. 3; Kröner et al. 1994; Hammer et al. 1999; Thomas et al.

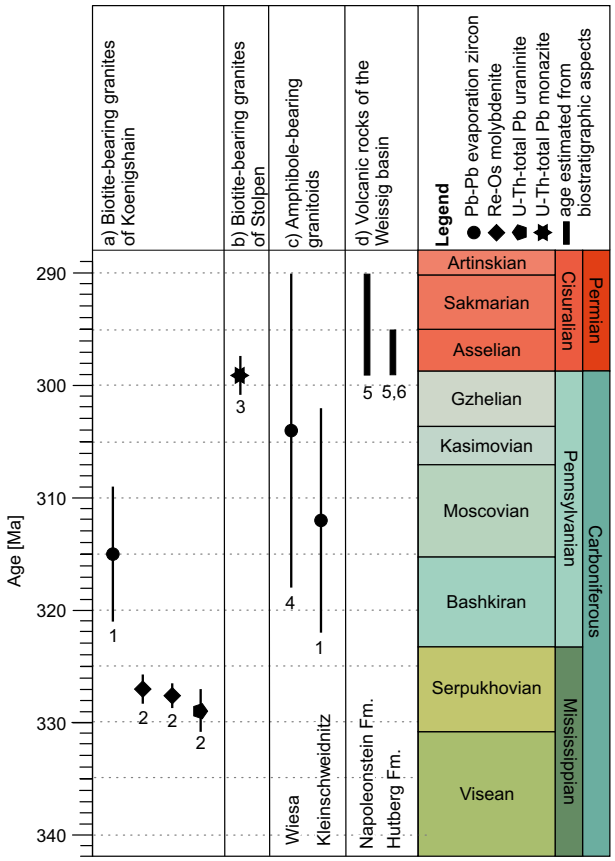

Fig. 3 Published age data from late- to post-Variscan granites of the German part of the Lusatian Block. Data are from (1) Hammer et al. (1999), (2) Förster et al. (2012), (3) Lisowiec et al. (2014), (4) Kröner et al. (1994), (5) Reichel et al. (2012), (6) Barthel et al. (2010)

2009; Förster, et al. 2012; Lisowiec et al. 2014). The age data span a range from 331 to 290 Ma and are partly contradictory. Consequently, the intrusion sequence of the granitoid rocks still has to be resolved (Fig. 3).

Variscan volcanic dykes of rhyolitic to rhyodacitic composition accompany and partly cross-cut the granite plutons of Stolpen and, to a lesser amount, of Koenigshain (Kozdrój et al. 2001; Fig. 2b, c). Near the Weissig basin and the Stolpen pluton, almost all dykes strike NW, roughly parallel to the EFZ. In addition, some dykes strike NE to ENE (Fig. 2b). Subordinate NE to ENE striking dykes prevail near the Koenigshain pluton (Fig. 2c). These dykes, the lavas, and tuffs from the Weissig basin have not yet been dated by radiometric methods. For the Weissig basin, age estimates based on fossil insect wings indicate an Asselian age for the sediments interlayered with volcanic rocks (Schneider and Werneburg 2012; Reichel 2012).

Materials and methods

Samples

This study aimed to acquire intrusion ages for Variscan igneous rocks of the northern Lusatian Block (Fig. 2b, c). Four samples were taken from the Koenigshain pluton (BGK1, BGK2, BGK3, BGK4) and three samples from the Stolpen pluton (BGSt11, BGSt13, BGSt14; Fig. 2b, c) to cover different textural varieties of the two biotite-bearing granitic plutons. From the amphibole-bearing granitoids, three samples from different drill holes were chosen (AG59, AG61, AG65; Fig. 2c). Exemplarily for the widespread rhyolitic and rhyodacitic dykes of the Lusatian Block, we sampled eight dykes around the Stolpen pluton (VR03, VR09, VR10, VR11, VR15, VR20, VR28, VR34; Fig. 2b). Most of the dyke samples represent loose blocks of rocks found at surface. From the Weissig basin, we selected a porphyritic tuff of the Napoleonstein Formation (VRW65) and a porphyritic lava from the Hutberg Formation (VRW67). Table 1 summarizes the sample numbers, localities, coordinates, and rock types of studied samples.

Bulk-rock geochemistry

18 out of 19 whole-rock samples were analysed for major and trace element contents at Activation Laboratories (Actlabs Canada; "4 Litho" research analytical protocol) by Fusion-ICP and Fusion-MS, respectively. Samples were fused with lithium metaborate/tetraborate and afterward diluted and analysed by Perkin Elmer Sciex ELAN 6000, 6100, or 9000 ICP/MS. Three blanks and five controls (three before the sample group and two after) were analysed per group of samples. Duplicates were fused and analysed every 15 samples. The instrument was recalibrated every 40 samples. Reproducibility was better than 1% for major elements and better than 5% for trace elements based on analyses of certified standards.

Zircon separation and dating

Zircons have been extracted from all 19 samples by the usual procedure (crushing, Wilfley table, Frantz magnetic separator, heavy liquids, final handpicking). The selected zircons were characterized using secondary electron (SE) images to evaluate their morphology. Cathodoluminescence (CL) images of the same grains visualize their internal structure. Energy-dispersive X-ray spectroscopy (EDX) was used to determine the elemental composition of mineral inclusions.

Table 1 Sample locations and description

Sample name	Sample number	Location name	Longitude (°E)	Latitude (°N)	Rock description
a) Biotite-bearing granites of Koenigshain					
BGK1	König1	Totenstein	14°50′56.5″	51°11′58.4″	Biotite-bearing granite
BGK2	König2	400 m SSE Hochstein	14°50′34.3″	51°11′43.1″	Biotite-bearing granite
BGK3	König3	Liebensteiner Höhe	14°53′22.5″	51°12′00.9″	Biotite-bearing granite
BGK4	Arn-Hil	quarry "Pro Stein"	14°46′37.4″	51°11′28.4″	Biotite-bearing granite
b) Biotite-bearing granites of Stolpen					
BGSt11	4_3/11	Karl-Lampe-Weg, N Knochenmühle, rock cliff	14°08′13.″	51°01′31.3″	Biotite-bearing granite
BGSt13	4_3/13	Karl-Lampe-Weg, convex riverbank	14°07′21.6″	51°00′55.7″	Biotite-bearing granite
BGSt14	4_3/14	"Das Hohe Birkigt", summit	14°09′33.4″	51°01′13.4″	Biotite-bearing granite
c) Amphibole-bearing granitoids					
AG59	KT 2/59	Drilling KT 2/59, depth: 15—50 m	14°54′24.9″	51°20′25.1″	Amphibole-bearing granite
AG61	Ob-Pr 1/61	Drilling Ober-Prauske 1/61, depth: 276—353 m	14°40′33.4″	51°15′41.6″	Amphibole-bearing granite
AG65	KLSW 1/65	Drilling Kleinschweidnitz 1/65, depth: 6—25 m	14°38′51.2″	51°04′20.8″	Amphibole-bearing granite
d) Volcanic rocks in dykes					
VR03	Groß 3	Wayside between Großensberg and Langenwolmsdorf, loose blocks of rock	14°07′30.2″	51°02′53.4″	Rhyolite
VR09	3_1/9	Railway bridge at "Wüste Mark Katharina", loose blocks of rock	14°03′41.0″	51°02′16.9″	Rhyolitic dike
VR10	3_2/10	N Niederhelmsdorf at the old quarry, loose blocks of rock	14°02′25.9″	51°02′36.4″	Rhyolitic dike
VR11	2_4/11	N Kleinerkmannsdorf, bus stop, loose blocks of rock on hill top	13°55′48.6″	51°04′49.7″	Porphyritic dike, trachyte
VR15	4_3/15	Karl-Lampe-Weg, NE Scheibenmühle	14°06′52.4"	51°00′18.9″	Rhyolitic dike
VR20	3_3/20	"Das Hohe Birkigt", Forstweg, N elevation point 345.9 m	14°09′17.2"	51°01′36.9″	Biotite-bearing microgranite, porphyritic
VR28	5_3/28	NW Bonnewitz	13°55′40.8″	51°00′50.7″	Porphyritic dike
VR34	4_6/34	W of Dürröhrsdorf, Hubertuskapelle, valley entrance	13°59′05.5″	51°02′10.3″	Cataclastic rhyolite, porphyrite
e) Volcanic rocks of the Weissig basin					
VRW65	3_4/65	Quarry SE Napoleonstein	13°55′08.4″	51°03′21.9″	Porphyritic tuff, trachytic andesite
VRW67	2_3/67	Quarry at Hutberg near Weissig	13°53′27.2″	51°03′50.4″	Porphyritic lava, trachytic andesite

Zircon U–Pb CA–ID–TIMS dating is a highly precise and accurate, but also time-consuming, laborious, and expensive method. A preceding sample selection, based on zircon characteristics like morphology and internal structure and a more rapid dating approach like zircon U–Pb LA–ICP–MS or the evaporation method, can be used to select the best suited samples for additional CA–ID–TIMS and SHRIMP dating. Here, we used the zircon evaporation method because this is a routine method in our laboratory.

Zircon dating by evaporation (Kober method)

All 19 samples were analysed with single zircon evaporation at TU Bergakademie Freiberg following the methods outlined by Kober (1987). Filament assemblies were mounted on a Finnigan MAT262 mass spectrometer. Before zircon evaporation, the second (ionization) filament was heated to 1800 °C to strip the filament from possible lead-bearing phases (additional outgassing). The evaporation filament was then heated to 1450 °C to remove common lead hosted in less stable phases of the zircon grain. Evaporation was performed at 1600 °C after cooling the ionization filament. This was done in one step to obtain high signal intensities for measurement. Data acquisition was performed by peak jumping using a secondary electron multiplier equipped with an ion counter with mass sequence 207–206–204–206–207 (counting time in seconds 4–4–8–4–4, respectively). A mean value was calculated from the two $^{207}Pb/^{206}Pb$ and $^{204}Pb/^{206}Pb$ ratios of each scan to minimize intensity changes during measurements. Ten blocks (composed of ten scans)

were recorded corresponding to 90 scans per measurement. Since $^{204}Pb/^{206}Pb$ ratios bear a large uncertainty due to the low intensity of ^{204}Pb, a trend line was defined through subsequently measured $^{204}Pb/^{206}Pb$ ratios.

Temora 2 was dated as a secondary standard as suggested by Horstwood et al. (2016; analytical data are given in Supplement 4). The mean evaporation age of secondary standard Temora 2 is with 419.3 ± 3.0 Ma ca. 1% older, but still within error identical to published values (416.8 ± 0.3 Ma, Black et al. 2003, 417.5 ± 0.1 Ma and 417.3 ± 0.1 Ma, von Quadt et al. 2016). According to these data and the primary standard 91500, the precision and accuracy of our zircon evaporation data is ca. 2% (Supplement 4).

Zircon U–Pb SHRIMP dating

Zircons from one sample (BGK1) were additionally analysed by the SHRIMP II technique (Sensitive High mass Resolution Ion MicroProbe) at the Centre of Isotopic Research (VSEGEI, St. Petersburg, Russia). Each analysis consisted of 5 scans through the mass range. The spot diameter was about 18 µm, and the primary beam intensity was about 4 nA. The data have been reduced in a manner similar to those used by Williams (1998, and references therein), using the SQUID Excel Macro of Ludwig (2000). The zircon standard Temora2 was used for reference of the U/Pb ratio and concentrations (Black et al. 2003). Primary standard data cannot test the accuracy of a dating method, because these standard data are used to calibrate the unknowns and match by definition the accepted values. Nevertheless, these data are valuable, because they illustrate the precision of the method. Therefore, we present primary standard values for SHRIMP (Temora2, Supplement 4, Tichomirowa et al. 2019a). Accordingly, the precision of our zircon U–Pb SHRIMP dating is at about 1–2% (see also Schaltegger 2015).

To trace the accuracy of any dating method, secondary reference materials should be dated together with the unknowns (Horstwood et al. 2016). Our SHRIMP data were acquired in 2011. This is the reason why a secondary standard was not analysed by the SHRIMP method.

Corrections for common lead (Pb_c) were made using measured ^{204}Pb and by applying the Pb evolution model of Stacey and Kramers (1975). Uncertainties given for individual analyses (ratios and ages) are at the 1σ level, for calculated Concordia ages at the 2σ level.

Zircon U–Pb CA–ID–TIMS dating

For this labour-intensive method, we chose 1–2 representative samples from each of the biotite-bearing granites of Koenigshain (BGK1, BGK4) and Stolpen (BGSt11, BGSt14), the amphibole-bearing granitoids (AG61), and the volcanic rocks of the Weissig basin (VRW67).

Selected zircon grains (ca. 30—50 per sample) were annealed for 72–96 h at 900 °C, and subsequently chemically abraded for 12 h at 210 °C with concentrated HF and HNO_3 in a pressurized Parr dissolution vessel. This procedure dissolves crystal domains with strong radiation damage which are suspected to have experienced post-crystallization lead loss (Mattinson 2005). The removal of Pb loss after application of this lab protocol has been proven for the Plešovice reference zircon but does not need to be appropriate equally for zircons from other samples (Widmann et al. 2019). Afterwards, the acid together with dissolved zircon material was completely pipetted out and 3.5N HNO_3 was added to the remaining zircons grains and fragments and left for 30 min at 50 °C to remove surface lead. Several cleaning cycles with water combined with repeated ultrasonic treatment were conducted before single zircon fragments were selected for further processing. Single zircon grains/fragments were washed with 3.5N HNO_3 and transferred into cleaned microcapsules with a small drop of this fluid and four drops of concentrated HF. Samples were spiked with a ^{205}Pb- ^{233}U-^{235}U- tracer solution (ET535 at TU Bergakademie Freiberg, Condon et al. 2015). For final dissolution, the microcapsules were placed in pressurized Parr dissolution vessels and heated to 200 °C for 48 h, followed by drying at 130 °C and then re-dissolution in 6N HCl for 24 h at 200 °C to transfer them into chlorides. After repeated drying, the samples were dissolved in ten drops of 3.1N HNO_3 and transferred into micro-columns for column chemistry. U and Pb were separated from the rest of the sample by anion exchange chromatography using HCl and H_2O. The U and Pb containing fraction was loaded on pre-degassed rhenium filaments with a drop of silica gel (Gerstenberger and Haase 1997) and measured with a Finnigan Mass Spectrometer MAT262 using a secondary electron multiplier (SEM). Alternatively, the samples were measured on an IsotopX Phoenix Mass Spectrometer using Daly ion counter and/or Faraday collectors (ATONA). The comparability of the results of both mass spectrometers was proven by repeated measurement of zircon standards 91500 (Wiedenbeck et al. 1995) and Temora (Black et al. 2004). The published ages of Temora2 are 416.8 ± 0.3 Ma (Black et al. 2003), 417.5 ± 0.1 Ma for SEM-measurements and 417.3 ± 0.1 Ma for measurements on Faraday cups (von Quadt et al., 2016). Our date of 417.3 ± 0.6 Ma (Supplement 4) perfectly matches these values. Few analyses of Temora 2 show older ages (418–431 Ma) that can be interpreted as the presence of slightly older zircon grains in the Temora diorite and were not used for the mean age calculation. Additionally, the accuracy of zircon U–Pb CA–ID–TIMS ages was monitored by dating the standard 91500. This standard was determined to be 1062.4 ± 0.4 Ma (Wiedenbeck et al. 1995) or 1063.6 ± 0.3 Ma (Schoene et al. 2006).

Our weighted mean $^{206}Pb/^{238}U$-age of 1064.6 ± 1.3 Ma (Supplement 4) is within 0.1% of the accepted values. Based on the results of standard dating, we presume the here presented CA–ID–TIMS ages to be accurate on the 0.1% level.

In contrast to Pb–Pb evaporation and U–Pb SHRIMP dating, the CA–ID–TIMS method is not calibrated by an external zircon sample (e.g. a calibrated zircon reference) but by a mixed U–Pb tracer solution. Currently, the use of precisely and accurately calibrated EARTHTIME tracers reduced the inter-laboratory bias to 0.1% (Condon et al. 2015). Consequently, the CA–ID–TIMS method can reliably yield accurate U–Pb dates (e.g., Schaltegger et al. 2015) if this well-calibrated tracer is used.

Bulk rock Sm- and Nd-isotopes

About 200 mg of powder from whole-rock was dissolved in 50% HF-12N HNO_3, then attacked with 8N HNO_3 and finally with 6N HCl. Samarium and neodymium were separated by ion-exchange resins. The isotope ratios were measured on a Finnigan MAT262 spectrometer and the quoted errors are given at the 2σ level. Concentrations of Sm and Nd were obtained by isotope dilution. The $^{143}Nd/^{144}Nd$ ratios were normalized to $^{146}Nd/^{144}Nd = 0.7219$ (DePaolo 1981). Sm-Nd model ages were calculated using the depleted mantle model (TDM, Liew and Hofmann 1988). The mean value for $^{143}Nd/^{144}Nd$ of the standard JNdi was 0.512098 ± 0.000010 (n = 8).

Zircon geochemistry: Hf- and O-isotope ratios

For sample BGK1, in addition to in situ U–Pb zircon ages analysed by SHRIMP, the Hf- and O-isotope composition was determined from the same spots on these zircon grains. Hafnium isotopes were measured on a Thermo-Finnigan Neptune multi-collector ICP–MS coupled to a Resonetics 193 nm ArF excimer laser (CompexPro 102, Coherent) system at Goethe-University Frankfurt (GUF) (Gerdes and Zeh 2006). Spots of 40 to 60 µm in diameter were ablated with a repetition rate of 5.5 Hz and an energy density of 5 J/cm^2 during 55 s of data acquisition. All data were adjusted relative to the JMC475 standard ($^{176}Hf/^{177}Hf = 0.282160$) and quoted uncertainties are quadratic additions of the within-run precision of each analysis and the reproducibility of JMC475 (2 SD = 0.0028%, $n = 6$). We verified the accuracy and external reproducibility by repeated analysis of the reference zircons, Temora and GJ-1. They yielded $^{176}Hf/^{177}Hf$ ratios of 0.282689 ± 0.000023 (2 SD, $n = 11$ for Temora), 0.282012 ± 0.000014 (2 SD, $n = 8$ for GJ-1). This is in perfect agreement with previously published results (e.g., Gerdes and Zeh 2006; Sláma et al. 2008) and with the LA-MC-ICP-MS long-term average (2006–2012) of GJ-1 (0.282010 ± 0.000025; $n > 800$) reference zircon at GUF.

Zircon oxygen isotopes were measured with the Cameca IMS 1280 multicollector ion microprobe at the Swedish Museum of Natural History (Heinonen et al. 2015), utilizing a ~ 2 nA Cs^+ primary ion beam together with a normal incidence low-energy electron gun for charge compensation, medium field magnification (~ 80x), and two Faraday detectors (channels L2 and H2) at a typical mass resolution of ~ 2500. Measurements were performed in pre-programmed chain analysis mode with automatic field aperture and entrance slit, centered on the ^{16}O signal. The magnetic field was locked using NMR regulation for the entire analytical session. Each data acquisition run comprised a 20 × 20 µm pre-sputter to remove the Au layer, followed by the centering steps, and 64 s of data integration performed using a non-rastered, ~ 10 × 10 µm spot. In the measurement chain, every set of four unknowns was followed by two bracketing analyses on the 91500 standard zircon. A $\delta^{18}O$ value of + 9.86‰ (SMOW, Wiedenbeck et al. 2004) was assumed for the 91500 zircon in data normalization, and small linear-drift corrections were applied to each session. External reproducibility of ± 0.3‰ (1 SD) based on measurements on the standards was propagated into the overall uncertainty for each analysis.

Results

Bulk rock geochemistry

Whole-rock geochemical data of 18 samples are presented in Table 2. Classification of the samples based on major element data is presented in Fig. 4. REE- and Multi-element diagrams are shown in Fig. 5.

All analysed magmatic and volcanic rocks are rich in SiO_2 (61–79 wt.%, Table 2), plotting in a TAS-diagram (Le Bas et al. 1986) from granodiorite and quartz monzonite to high-SiO_2-granite and from trachydacite and dacite to rhyolite, respectively (Fig. 4a). The biotite-bearing granites of the Koenigshain and the Stolpen plutons plot at the high-SiO_2-end (76–78 wt.% SiO_2) and the amphibole-bearing granitoids generally have lower SiO_2 contents and reveal a greater variability from 64 to 69 wt.% SiO_2. These rocks are mainly classified as granodiorites and quartz-monzonites. The rhyolitic to trachydacitic volcanic dykes vary over a wider range of SiO_2 contents (65–79 wt.%), whereby some rhyolitic dykes are slightly more SiO_2-rich then the granitic rocks (Fig. 4a). The volcanic layers of the Weissig basin reveal similar SiO_2 contents (61–67 wt.%) and are classified as dacite and trachyte (Fig. 4a).

The Na_2O/K_2O-ratio of all samples is ≤ 1.3 for all rocks, classifying them as high-K calc-alkaline to shoshonitic rocks

Table 2 Whole-rock major and trace element contents

	a) Biotite-bearing granites of Koenigshain			b) Biotite-bearing granites of Stolpen			c) Amphibole -bearing granitoids			d) Volcanic rocks in dykes							e) Volcanic rocks of the Weissig basin	
	BGK2	BGK3	BGK4	BGSt11	BGSt13	BGSt14	AG61	AG59	AG65	VR34	VR28	VR09	VR10	VR15	VR11	VR20	VR65	VR67
wt-%																		
SiO_2	76.17	76.25	75.88	76.78	76.26	76.87	69.00	67.00	64.20	74.33	78.62	76.35	77.31	78.92	67.10	64.93	67.16	61.07
Al_2O_3	12.17	12.10	12.03	12.09	11.65	12.54	14.05	15.62	16.60	12.02	11.54	11.81	11.85	12.04	14.85	15.09	14.16	15.24
Fe_2O_3	0.99	0.98	1.40	1.70	1.62	1.77	2.83	3.32	4.41	1.78	1.35	0.95	1.12	0.99	3.39	5.98	5.59	6.79
MnO	0.018	0.022	0.025	0.015	0.018	0.026	0.044	0.047	0.067	0.013	0.011	0.005	0.008	0.007	0.021	0.085	0.067	0.059
MgO	0.10	0.03	0.09	0.13	0.08	0.12	0.94	1.61	1.89	0.26	0.09	0.05	0.05	0.14	0.53	0.82	1.05	1.45
CaO	0.53	0.40	0.58	0.15	0.35	0.54	1.67	2.72	3.91	0.04	0.07	0.07	0.08	0.10	0.11	2.23	0.52	1.00
Na_2O	3.76	3.81	3.39	3.26	3.29	3.24	2.74	3.32	3.80	1.53	1.84	2.59	3.21	3.97	2.22	3.25	4.01	3.34
K_2O	4.37	4.53	4.52	4.86	4.71	4.64	4.73	4.59	3.03	6.81	5.51	5.74	5.04	4.25	7.31	4.76	3.14	4.79
TiO_2	0.078	0.038	0.113	0.097	0.092	0.150	0.464	0.537	0.672	0.183	0.062	0.051	0.053	0.063	0.350	0.960	0.849	1.321
P_2O_5	0.030	0.040	0.050	0.005	0.005	0.030	0.130	0.160	0.170	0.050	0.030	0.020	0.030	0.020	0.060	0.320	0.320	0.490
Total	98.22	98.20	98.08	99.09	98.08	99.93	96.60	98.92	98.75	97.02	99.12	97.64	98.75	100.50	95.94	98.43	96.87	95.55
A/CNK	1.02	1.02	1.04	1.11	1.05	1.11	1.11	1.02	1.00	1.21	1.27	1.11	1.09	1.06	1.26	1.04	1.29	1.22
ppm																		
V	7	< 5	7	7	7	11	35	68	69	9	< 5	7	8	6	10	60	51	128
Ga	21	21	18	20	21	20	17	19	20	14	17	21	17	22	20	24	20	21
Ge	3	3	2	2	2	2	1	< 1	1	1	< 1	1	< 1	2	1	1	1	< 1
Rb	263	337	183	240	290	279	154	190	101	181	330	301	198	210	190	147	81	133
Sr	36	3	23	23	27	48	78	481	482	29	14	24	29	19	42	200	45	140
Y	42	48	29	40	46	36	40	26	22	41	47	60	51	46	39	54	38	42
Zr	82	90	153	108	117	147	209	292	205	249	101	90	93	90	375	516	430	392
Nb	31	34	18	23	27	21	8	16	9	17	16	21	20	15	26	36	21	23
Ag	< 0.5	< 0.5	0.5	0.6	0.6	0.6	0.8	1.0	0.8	1.1	0.9	0.5	< 0.5	< 0.5	1.3	1.4	1.1	1.1
Sn	5	9	4	4	4	4	3	2	3	6	6	10	8	14	10	4	3	4
Cs	4.9	10.9	4.1	1.8	2.2	2.9	6.3	5.1	3.0	1.3	4.5	1.5	1.2	0.9	2.7	< 0.5	0.9	1.3
Ba	142	9	100	105	82	255	665	1355	917	595	127	83	213	110	1567	1160	615	1006
Hf	4.1	4.9	5.4	4.3	5.0	5.3	5.2	7.6	4.9	6.5	3.9	4.7	4.6	4.3	9.1	12.7	9.6	9.1
Ta	3.9	3.7	1.8	2.5	3.5	2.7	0.9	1.6	1.0	1.6	1.8	2.8	2.7	2.1	1.6	2.1	1.6	1.7
Tl	1.3	1.8	0.9	1.0	1.4	1.2	0.8	1.0	0.5	1.5	2.2	1.5	1.2	1.1	1.2	0.7	0.5	0.7
Pb	40	44	32	14	25	23	20	25	15	< 5	9	13	11	8	< 5	18	10	< 5
Th	33.6	34.6	40.9	26.2	26.0	26.8	12.1	42.4	14.0	20.4	42.5	46.3	45.0	49.6	18.0	17.6	14.6	13.4
U	10.5	13.4	9.4	3.5	4.5	5.2	3.9	11.0	4.3	3.4	5.5	9.3	7.8	7.7	3.7	3.4	3.3	2.7
Sc	5	5	3	n.a	n.a	n.a	8	8	10	5	5	n.a	n.a	n.a	9	13	11	14
La	20.5	12.0	36.4	20.1	27.2	41.2	33.0	63.5	36.3	43.2	23.0	17.4	21.3	30.0	50.3	91.3	83.7	46.0

Table 2 (continued)

	a) Biotite-bearing granites of Koenigshain			b) Biotite-bearing granites of Stolpen			c) Amphibole -bearing granitoids			d) Volcanic rocks in dykes							e) Volcanic rocks of the Weissig basin	
	BGK2	BGK3	BGK4	BGSt11	BGSt13	BGSt14	AG61	AG59	AG65	VR34	VR28	VR09	VR10	VR15	VR11	VR20	VR65	VR67
Ce	46.3	31.4	75.9	45.6	60.7	83.8	69.0	115.0	69.6	85.0	60.1	42.3	47.7	65.8	90.4	168.0	152.0	88.9
Pr	5.71	4.27	8.37	5.64	7.72	9.67	8.07	11.80	7.78	10.20	7.45	5.75	6.63	8.64	11.50	20.10	18.40	11.30
Nd	22.7	17.9	30.7	21.4	28.4	34.1	30.8	40.1	27.9	36.9	30.2	23.5	25.6	32.5	40.0	72.0	65.7	43.4
Sm	6.8	6.6	6.4	5.3	7.3	7.1	6.5	6.8	5.1	7.5	8.2	7.2	7.6	8.7	7.1	13.0	11.5	8.2
Eu	0.15	<0.05	0.23	0.22	0.16	0.38	1.02	1.41	1.26	0.94	0.19	0.14	0.36	0.39	1.10	2.35	2.09	1.61
Gd	6.7	6.8	5.6	4.9	6.8	5.7	6.1	4.9	4.5	7.0	7.5	7.6	7.3	8.3	5.3	11.2	8.8	7.6
Tb	1.3	1.4	0.9	1.0	1.3	1.1	1.0	0.7	0.7	1.2	1.4	1.5	1.4	1.6	0.9	1.7	1.2	1.2
Dy	7.7	8.5	5.2	6.4	8.5	6.4	6.3	4.0	3.7	7.3	8.6	9.9	9.0	9.5	6.2	9.7	6.9	6.9
Ho	1.5	1.7	1.0	1.3	1.8	1.3	0.7	0.8	1.3	1.4	1.7	2.0	1.8	1.8	1.3	1.9	1.3	1.4
Er	4.4	5.1	3.0	4.0	5.3	3.9	3.7	2.2	2.1	4.2	5.0	5.9	5.2	5.1	3.7	5.7	4.0	4.1
Tm	0.69	0.82	0.47	0.69	0.92	0.67	0.54	0.34	0.31	0.64	0.81	0.98	0.86	0.85	0.55	0.81	0.56	0.60
Yb	4.9	5.5	3.1	4.4	5.7	4.3	3.4	2.2	2.0	4.2	5.1	6.2	5.4	5.2	3.5	5.1	3.5	3.6
Lu	0.74	0.81	0.52	0.62	0.83	0.62	0.49	0.32	0.29	0.67	0.79	0.88	0.73	0.74	0.51	0.76	0.53	0.54
$(La/Yb)_N$	0.27	0.14	0.76	0.29	0.31	0.62	0.63	1.86	1.17	0.66	0.29	0.18	0.25	0.37	0.29	1.15	1.54	0.82
Eu/Eu*	0.10	n.a	0.17	0.19	0.10	0.26	1.14	1.06	0.70	0.56	0.11	0.08	0.21	0.20	0.19	0.84	0.90	0.88
T^1 [°C]	734	741	788	764	766	790	814	828	788	847	772	751	751	746	882	885	899	873
T^2 [°C]	745	658	785	769	767	809	897	900	913	831	725	698	703	722	869	948	944	972

1)Zircon saturation temperatures according to Watson and Harrison (1983)

2)Magma temperatures calculated according to Jung and Pfänder (2007)

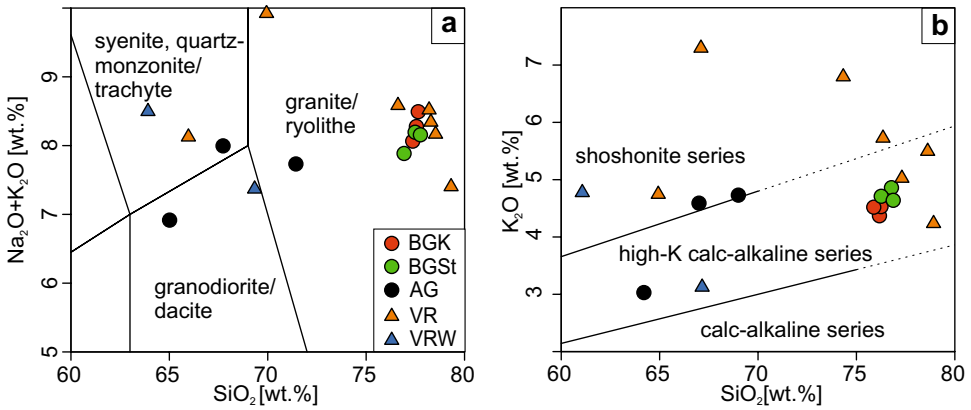

Fig. 4 Geochemical classification of the investigated samples based on whole-rock major element data. **a** Total-alkali-silica (TAS) diagram according to Le Bas et al. (1986), based on analyses recalculated on volatile-free basis, **b** SiO_2-K_2O plot according to Peccerillo and Taylor (1976). The sample groups are *BGK* biotite-bearing granite of the Koenigshain pluton, *AG* amphibole-bearing granite, *BGSt* biotite-bearing granite of the Stolpen pluton, *VR* volcanic rocks in dykes, *VRW* volcanic rocks within the Weissig basin

(Fig. 4b: K_2O vs. SiO_2 diagram, Peccerillo and Tailor 1976). In this diagram, biotite-bearing granites are restricted to the high-K calc-alkaline field, but amphibole-bearing granitoids reveal a wider dispersion from the high-K calc-alkaline to the shoshonitic field. Volcanic dykes show the widest scatter with the highest K_2O contents in some samples. All analysed rocks are peraluminous with A/CNK [Al_2O_3/($CaO + Na_2O + K_2O$)] ranging from 1.0 to 1.3.

The REE patterns of the biotite-bearing granites of Koenigshain and Stolpen and some of the volcanic dykes show, compared to the upper continental crust (UCC, Rudnick and Gao 2014), a significant negative Eu-anomaly (0.1–0.3, Table 2, Fig. 5a). In these samples, all other REE contents are similar to the upper continental crust with a slight enrichment of the HREE (LaN/YbN-ratios = 0.1–0.8, Table 2). The amphibole-bearing rocks, the volcanic rocks of the Weissig basin, and three volcanic dykes have only weakly negative or absent Eu-anomalies (Eu*/Eu = 0.7–1.1, Table 2) and do not show an enrichment of HREE over LREE compared to UCC (LaN/YbN = 0.6–1.9, Table 2). Their absolute REE contents are similar to that of the upper continental crust, or shifted towards slightly higher contents.

In upper-continental-crust-normalized multi-element diagrams (Fig. 5, Rudnick and Gao 2014), the biotite-bearing granites of Koenigshain and Stolpen and most of the volcanic dykes are slightly enriched in LILE and show significant negative anomalies of Ba, Sr, Ca, Eu, Zr, and Ti. The negative anomalies of Sr and Ca are only weakly pronounced in the amphibole-bearing rocks and one volcanic dyke and show intermediate values for the volcanic rocks of the Weissig basin and two volcanic dykes. The negative Eu, Ba, and Zr anomalies are mostly absent in these rocks.

From bulk rock geochemical data, we calculated crystallization temperatures according to Watson and Harrison (1983) and according to Jung and Pfänder (2007; Table 2). The scarcity of inherited zircons (Tables 3, 4, Supplement 1) in most samples allows for the calculation of zircon saturation temperatures (Watson and Harrison 1983) as melt temperatures estimates. With both methods, the crystallization temperatures for the biotite-bearing granites of the Koenigshain and Stolpen plutons are roughly identical with 734–790 °C for the zircon saturation temperatures (Watson and Harrison 1983) and 658–809 °C according to Jung and Pfänder (2007). The amphibole-bearing granites revealed higher temperatures for both geothermometers with 788–828 °C (Watson and Harrison 1983) and 897–913 °C (Jung and Pfänder 2007). The calculated temperatures of the volcanic dykes roughly vary with SiO_2 content (Fig. 6). For volcanic dykes with $SiO_2 < 75$ wt.%, the calculated temperatures according to Watson and Harrison (1983) resulted in 847–899 °C indicating even higher temperatures compared to those for amphibole-bearing granitoids, while similar temperatures result from calculations according to Jung and Pfänder (2007, 831–972 °C). Volcanic rocks with $SiO_2 > 75$ wt.% have zircon saturation temperatures of 746 to 772 °C and magma temperatures of 698–725 °C that overlap with those temperatures calculated with the same methodology for the biotite-bearing granites of the Stolpen and Koenigshain plutons.

Zircon ages

Zircon characterization and Pb–Pb evaporation age determination

Following zircon characterization, single-grain zircon Pb–Pb evaporation was performed on selected grains of each sample. Figure 7 shows representative SE and CL images of

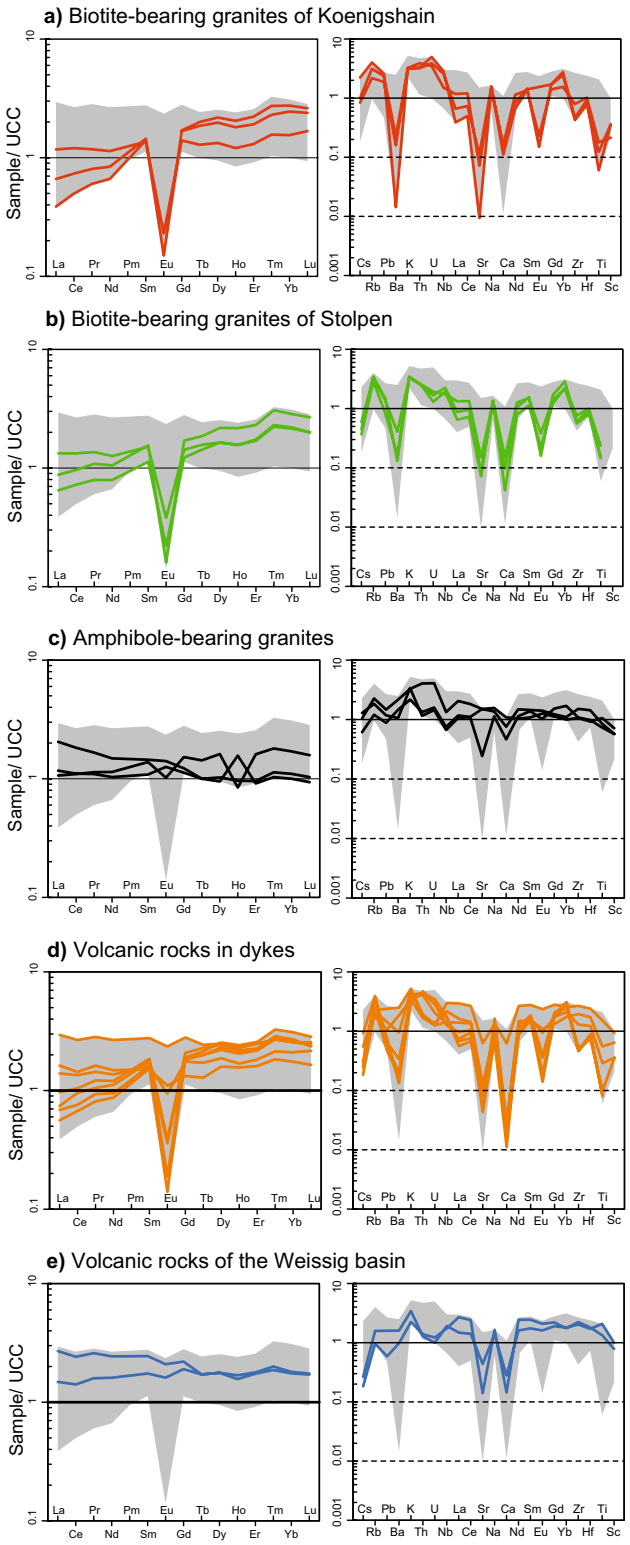

Fig. 5 Upper continental crust (UCC, Rudnick and Gao, 2013) normalized REE patterns (left column) and multi-element patterns (right column). The data for each sample are shown as a coloured lines. For better comparison between **a**–**e**, the range covered by all samples is shown as grey shaded area in all plots

Table 3 Single spot zircon U–Pb SHRIMP dates and isotopic data of sample BGK1

Fraction_grain.spot	U (ppm)	Th (ppm)	$^{206}Pb^*$ (ppm)	$^{232}Th/^{238}U$	f $^{206}Pb_c$ [a] (%)	$^{207}Pb^*/^{206}Pb^*$	± 1σ [b] (%)	$^{207}Pb^*/^{235}U$	± 1σ [b] (%)	$^{206}Pb^*/^{238}U$	± 1σ [b] (%)	Corr Coeff	Disc (%)	$^{206}Pb^*/^{238}U$ age (Ma)	± 1σ (abs.)
Kö_1.1	121	77	5.3	0.66	0.00	0.0545	2.83	0.3840	3.09	0.0511	1.24	0.40	18.9	321.1	3.9
Kö_4.1	196	214	8.6	1.13	0.00	0.0542	2.98	0.3810	3.18	0.0510	1.12	0.35	15.4	320.8	3.5
Kö_5.1	190	178	8.3	0.97	0.00	0.0560	2.96	0.3941	3.17	0.0511	1.11	0.35	29.7	321.0	3.5
Kö_6.1	264	273	12	1.06	0.00	0.0522	1.84	0.3691	2.13	0.0513	1.07	0.50	− 10.4	322.6	3.4
Kö_2.1	566	181	25	0.33	0.00	0.0528	1.54	0.3737	1.85	0.0513	1.01	0.55	− 0.7	322.6	3.2
Kö_3.1	205	172	9.1	0.87	0.00	0.0568	2.77	0.4024	3.05	0.0514	1.28	0.42	34.2	322.9	4.0
Kö_5.1	194	187	8.6	0.99	0.14	0.0494	3.23	0.3503	3.42	0.0514	1.12	0.33	− 93.2	323.0	3.5
Kö_9.1	390	417	17	1.10	0.00	0.0532	1.51	0.3793	1.79	0.0517	0.97	0.54	3.3	325.2	3.1
Kö_8.1	349	151	16	0.45	0.00	0.0514	1.63	0.3677	1.91	0.0519	0.99	0.52	− 26.0	325.9	3.1
Kö_7.1	755	369	34	0.51	0.00	0.0549	5.14	0.3936	5.22	0.0520	0.94	0.18	20.4	326.8	3.0
Kö_10.1	231	219	10	0.98	0.00	0.0546	1.90	0.3920	2.16	0.0520	1.02	0.47	18.3	326.9	3.2

Pbc and Pb* indicate the common and radiogenic portions, respectively

a—fraction (%) of common Pb

b—error in standard calibration was 0.50% (not included in above errors but required when comparing data from different mounts)

Table 4 U–Pb CA-ID-TIMS single-grain zircon dates and isotopic data

Fraction and sample	Dates [Ma]								Composition			Isotopic Ratios						
	$^{206}Pb/^{238}U$	±2σ	$^{207}Pb/^{235}U$	±2σ	$^{207}Pb/^{206}Pb$	±2σ	Corr	%disc	Pb*	Pb_c	Pb*/Pb_c	$^{206}Pb/^{204}Pb$	$^{206}Pb/^{238}U$	±2σ	$^{207}Pb/^{235}U$	±2σ	$^{207}Pb/^{206}Pb$	±2σ
	a	(abs.)	a	(abs.)	a	(abs.)	Coeff	b	c	d	e	f	g	(%)	g	(%)	g	(%)
a) Biotite-bearing granites of Koenigshain																		
BGK1																		
2	310.4	0.4	312.0	4.3	324	36	0.07	4.11	43.6	3.6	12.2	724	0.0493	0.13	0.3597	1.60	0.0529	1.60
4	316.2	1.2	323.4	7.9	376	63	0.16	15.8	25.7	3.9	6.55	403	0.0503	0.40	0.3751	2.86	0.0541	2.82
7	315.1	1.2	313.0	7.9	298	65	0.20	-5.77	22.7	3.4	6.76	395	0.0501	0.37	0.3611	2.92	0.0523	2.87
8	312.9	0.4	315.5	5.2	335	44	0.04	6.53	33.7	3.3	10.1	603	0.0497	0.12	0.3644	1.93	0.0532	1.93
9	312.6	0.4	315.1	5.4	334	45	0.05	6.34	35.1	3.5	10.1	584	0.0497	0.13	0.3638	2.00	0.0531	1.99
11	308.6	0.7	310.2	4.7	322	40	0.13	4.25	53.7	4.8	11.1	655	0.0490	0.24	0.3574	1.77	0.0529	1.75
g-1	316.4	0.7	320.0	9.5	347	78	0.03	8.76	16.7	3.1	5.32	344	0.0503	0.22	0.3705	3.44	0.0534	3.44
g-2	314.5	0.3	314.2	4.4	312	37	0.04	-0.73	42.9	3.3	12.9	723	0.0500	0.10	0.3627	1.61	0.0526	1.61
g-3	312.6	0.4	315.1	3.4	333	28	0.13	6.22	60.2	4.0	15.0	909	0.0497	0.13	0.3638	1.25	0.0531	1.24
k-1	312.9	0.4	315.8	5.1	337	42	0.06	7.16	38.1	3.6	10.5	608	0.0497	0.14	0.3648	1.88	0.0532	1.87
k-2	313.7	0.5	317.0	6.4	341	53	0.06	7.95	25.4	3.0	8.51	496	0.0499	0.15	0.3664	2.34	0.0533	2.34
k-3	315.2	1.1	319.6	17.9	352	148	0.01	10.5	10.6	3.6	2.97	190	0.0501	0.36	0.3699	6.55	0.0536	6.55
k-4	314.2	0.4	310.5	5.2	282	44	0.03	-11.2	31.5	3.0	10.5	608	0.0500	0.12	0.3577	1.93	0.0520	1.93
k-5	310.3	0.7	301.2	7.8	231	69	0.01	-34.1	22.1	3.3	6.66	402	0.0493	0.22	0.3453	2.98	0.0508	2.99
BGK4																		
1	307.0	1.5	306.0	22.0	295	186	0.01	-4.09	70.3	29	2.44	160	0.0488	0.49	0.3512	8.13	0.0522	8.14
2	312.2	0.4	314.1	5.5	329	47	0.03	5.08	33.3	3.4	9.80	570	0.0496	0.14	0.3626	2.05	0.0530	2.05
3	312.8	0.4	315.1	3.1	332	26	0.03	5.83	62.2	3.7	16.6	974	0.0497	0.12	0.3638	1.13	0.0531	1.13
4	311.7	0.3	314.6	3.2	336	27	0.07	7.31	58.4	3.5	16.6	967	0.0495	0.10	0.3632	1.19	0.0532	1.18
5	302.4	0.4	304.3	3.4	318	29	0.09	5.00	167	11	15.0	897	0.0480	0.12	0.3494	1.29	0.0528	1.28
6	310.8	0.5	312.9	0.4	328	0	1.00	5.36	221	3.4	64.8	3915	0.0494	0.17	0.3609	0.16	0.0530	0.00
7	312.4	0.2	312.9	0.9	317	7	0.26	1.35	203	3.6	56.9	3414	0.0497	0.06	0.3610	0.33	0.0527	0.32
8	310.9	0.3	312.4	1.0	324	8	0.27	4.11	158	3.5	45.8	2624	0.0494	0.09	0.3603	0.37	0.0529	0.35
9	308.6	0.2	310.3	0.9	323	8	0.22	4.60	177	3.2	55.2	3270	0.0490	0.06	0.3575	0.35	0.0529	0.34
10	304.1	0.7	305.5	1.0	316	7	0.61	3.69	192	3.3	58.8	3400	0.0483	0.24	0.3510	0.39	0.0527	0.31
11	316.0	0.5	315.8	7.4	314	62	0.00	-0.71	24.6	3.4	7.18	432	0.0502	0.16	0.3647	2.74	0.0527	2.74
12	314.4	0.4	314.9	6.5	318	55	0.02	1.27	45.1	5.6	8.03	491	0.0500	0.14	0.3636	2.40	0.0528	2.40
14	310.7	0.3	312.6	1.2	327	10	0.25	4.91	158	3.7	42.7	2617	0.0494	0.09	0.3606	0.44	0.0530	0.43
15	313.0	0.2	313.6	2.0	318	17	0.15	1.61	80.1	3.1	25.7	1568	0.0498	0.08	0.3619	0.74	0.0528	0.73
16	308.4	0.4	309.0	3.7	314	32	0.05	1.70	40.5	3.0	13.5	814	0.0490	0.13	0.3558	1.39	0.0527	1.39
17	312.0	0.3	313.4	3.2	324	27	0.04	3.81	51.9	3.3	15.6	954	0.0496	0.09	0.3616	1.20	0.0529	1.20
18	312.8	0.3	313.9	2.4	322	20	0.02	2.84	60.6	2.8	21.6	1259	0.0497	0.09	0.3622	0.89	0.0529	0.89

Table 4 (continued)

Fraction and sample	Dates [Ma]								Composition			Isotopic Ratios						
	$^{206}Pb/^{238}U$	±2σ	$^{207}Pb/^{235}U$	±2σ	$^{207}Pb/^{206}Pb$	±2σ	Corr	%disc	Pb*	Pb_c	Pb*/Pb_c	$^{206}Pb/^{204}Pb$	$^{206}Pb/^{238}U$	±2σ	$^{207}Pb/^{235}U$	±2σ	$^{207}Pb/^{206}Pb$	±2σ
	a	(abs.)	a	(abs.)	a	(abs.)	Coeff	b	c	d	e	f	g	(%)	g	(%)	g	(%)
b-1	312.9	0.3	312.5	3.0	310	25	0.04	-0.93	51.9	3.0	17.4	1038	0.0497	0.08	0.3604	1.11	0.0526	1.11
b-2	313.1	0.3	302.8	5.3	224	47	0.23	-39.8	33.5	3.4	9.80	585	0.0498	0.10	0.3475	2.01	0.0507	2.04
b-3	312.8	0.2	311.7	1.7	304	14	0.07	-2.97	76.7	2.7	28.0	1687	0.0497	0.07	0.3593	0.63	0.0524	0.63
b-4	311.2	0.6	308.7	3.6	290	31	0.02	-7.37	41.5	3.0	13.7	809	0.0495	0.18	0.3553	1.34	0.0521	1.34
b-5	313.4	0.4	312.9	6.4	309	54	0.02	-1.48	39.0	5.0	7.81	501	0.0498	0.14	0.3609	2.36	0.0526	2.36
b-6	313.9	0.4	317.3	5.0	342	41	0.06	8.27	31.4	3.0	10.5	635	0.0499	0.13	0.3669	1.83	0.0533	1.82
b) Biotite-bearing granites of Stolpen																		
BGSt11																		
a-1	298.2	0.4	298.2	5.7	298	50	0.03	0.05	39.5	4.5	8.85	539	0.0473	0.13	0.3414	2.20	0.0523	2.20
a-2	296.3	0.5	297.2	6.8	305	60	0.03	2.78	33.0	4.6	7.22	448	0.0470	0.16	0.3401	2.65	0.0525	2.65
a-3	318.2	0.9	319.6	14.2	330	117	0.04	3.52	11.8	3.3	3.54	237	0.0506	0.30	0.3700	5.16	0.0530	5.16
a-4	323.3	0.8	324.2	11.7	331	96	0.02	2.36	17.3	3.9	4.46	287	0.0514	0.24	0.3762	4.21	0.0531	4.21
a-6	298.2	0.5	300.9	7.7	321	67	0.04	7.16	23.6	3.4	6.92	402	0.0474	0.18	0.3449	2.96	0.0528	2.96
a-7	297.0	0.4	299.5	5.1	318	44	0.06	6.70	50.6	5.1	9.91	601	0.0472	0.15	0.3430	1.95	0.0528	1.95
b-1	296.8	0.3	299.3	2.0	319	18	0.15	7.07	101	4.2	24.4	1456	0.0471	0.11	0.3429	0.79	0.0528	0.78
b-2	296.8	0.3	299.5	3.2	321	28	0.09	7.45	54.2	3.3	16.4	949	0.0471	0.11	0.3430	1.22	0.0528	1.22
b-4	294.5	0.3	298.7	1.2	331	10	0.30	11.1	129	2.9	44.4	2583	0.0467	0.12	0.3420	0.45	0.0531	0.43
b-5	298.5	0.5	298.4	5.4	297	48	0.06	-0.36	31.9	3.5	9.19	566	0.0474	0.17	0.3416	2.10	0.0523	2.09
b-7	294.8	0.3	292.4	2.4	273	22	0.11	-8.04	66.3	3.3	19.9	1204	0.0468	0.10	0.3337	0.95	0.0517	0.94
BGSt14																		
1	296.0	0.3	298.2	1.2	315	10	0.21	6.12	134	3.2	42.2	2492	0.0470	0.10	0.3414	0.45	0.0527	0.44
3	296.9	0.3	299.7	1.5	322	13	0.23	7.72	111	3.2	34.7	1952	0.0471	0.10	0.3433	0.58	0.0529	0.56
4	296.8	0.4	299.4	5.0	319	44	0.03	7.07	53.1	5.1	10.3	600	0.0471	0.13	0.3430	1.94	0.0528	1.94
5	298.4	0.3	299.0	3.8	304	34	0.04	1.89	51.4	3.7	13.7	793	0.0474	0.10	0.3424	1.47	0.0525	1.47
6	297.9	0.3	299.0	3.2	307	28	0.14	3.06	54.2	3.7	14.8	917	0.0473	0.10	0.3424	1.24	0.0525	1.23
7	298.2	0.4	298.6	5.2	301	46	0.03	1.09	36.5	3.8	9.62	584	0.0473	0.13	0.3418	2.01	0.0524	2.01
b-1	296.7	0.3	298.1	3.2	309	28	0.08	3.96	54.5	3.3	16.4	938	0.0471	0.11	0.3412	1.24	0.0526	1.24
b-2	297.1	0.3	299.2	3.1	316	27	0.07	5.85	50.0	3.2	15.7	944	0.0472	0.10	0.3427	1.19	0.0527	1.19
b-3	296.3	0.6	298.2	1.4	313	12	0.27	5.34	140	3.6	38.5	2198	0.0470	0.20	0.3413	0.53	0.0527	0.51
b-4	299.1	0.4	300.1	6.5	308	57	0.02	2.79	65.5	8.6	7.64	475	0.0475	0.15	0.3438	2.50	0.0525	2.50
b-5	298.6	0.3	298.2	2.6	295	23	0.06	-1.11	55.4	3.1	17.9	1101	0.0474	0.11	0.3414	1.02	0.0522	1.02

Table 4 (continued)

Fraction and sample	Dates [Ma]								Composition			Isotopic Ratios						
	$^{206}Pb/^{238}U$ a	±2σ (abs.)	$^{207}Pb/^{235}U$ a	±2σ (abs.)	$^{207}Pb/^{206}Pb$ a	±2σ (abs.)	Corr Coeff	%disc b	Pb* c	Pb_c d	Pb^*/Pb_c e	$^{206}Pb/^{204}Pb$ f	$^{206}Pb/^{238}U$ g	±2σ (%)	$^{207}Pb/^{235}U$ g	±2σ (%)	$^{207}Pb/^{206}Pb$ g	±2σ (%)
c) Amphibole-bearing granitoids																		
AG61																		
1	312.2	0.3	314.7	3.4	333	28	0.08	6.22	53.4	3.4	15.5	911	0.0496	0.11	0.3633	1.26	0.0531	1.25
2	405.0	0.5	413.0	3.7	458	24	0.11	11.5	53.9	3.5	15.5	979	0.0648	0.12	0.5019	1.10	0.0562	1.10
3	466.1	0.4	474.1	3.1	513	18	0.11	9.19	66.1	3.3	20.2	1306	0.0750	0.09	0.5951	0.81	0.0576	0.80
4	312.9	0.5	316.0	7.4	338	62	0.03	7.48	27.4	3.8	7.16	432	0.0497	0.17	0.3650	2.72	0.0532	2.72
5	312.5	0.4	313.9	5.5	324	46	0.06	3.62	37.8	4.0	9.55	578	0.0497	0.15	0.3623	2.02	0.0529	2.02
6	356.0	1.6	368.4	24.7	447	178	0.01	20.4	12.3	5.4	2.28	153	0.0568	0.46	0.4374	7.99	0.0559	7.99
7	308.8	0.4	310.6	5.8	324	49	0.04	4.74	38.9	4.5	8.70	537	0.0491	0.14	0.3578	2.16	0.0529	2.16
8	469.9	0.5	474.9	4.3	499	25	0.09	5.81	50.1	3.4	14.7	953	0.0756	0.12	0.5963	1.12	0.0572	1.12
9	309.0	0.2	310.7	2.5	324	21	0.09	4.62	74.4	3.6	20.9	1247	0.0491	0.07	0.3580	0.92	0.0529	0.92
b-2	537.7	0.3	539.0	2.0	545	10	0.13	1.26	109	3.4	32.3	2130	0.0870	0.06	0.7004	0.48	0.0584	0.48
b-3	312.0	0.3	299.8	3.3	206	30	0.07	-51.4	68.2	4.5	15.1	912	0.0496	0.10	0.3435	1.28	0.0503	1.28
b-5	311.9	0.4	309.5	5.2	292	45	0.04	-7.00	151	15	10.1	603	0.0496	0.13	0.3564	1.95	0.0522	1.95
b-7	313.4	0.5	315.2	5.4	329	45	0.03	4.77	28.0	2.9	9.57	580	0.0498	0.15	0.3641	1.98	0.0530	1.98
b-8	314.7	0.4	314.8	4.6	316	39	0.04	0.35	59.2	5.1	11.5	680	0.0500	0.12	0.3635	1.71	0.0527	1.71
d) Volcanic rocks of the Weissig basin																		
VR67																		
1	299.0	0.7	301.9	10.3	325	89	0.02	7.87	17.8	3.4	5.32	307	0.0475	0.23	0.3462	3.93	0.0529	3.93
2	299.7	0.8	296.3	13.4	270	119	0.01	-11.1	15.2	3.9	3.87	242	0.0476	0.28	0.3389	5.21	0.0517	5.21
3	302.6	1.0	306.2	14.7	334	126	0.03	9.29	13.3	3.8	3.52	222	0.0481	0.32	0.3519	5.55	0.0531	5.55
4	298.8	0.5	295.0	8.2	265	73	0.02	-12.7	30.0	4.4	6.87	382	0.0474	0.18	0.3372	3.20	0.0516	3.20
5	298.3	0.5	301.5	6.3	327	55	0.03	8.64	29.6	3.3	8.88	487	0.0474	0.16	0.3458	2.42	0.0530	2.42
6	298.3	0.4	301.2	6.4	324	56	0.03	7.98	47.8	5.3	8.99	479	0.0474	0.15	0.3454	2.46	0.0529	2.46
7	299.3	0.9	297.9	12.7	288	112	0.02	-4.05	12.5	3.1	4.08	249	0.0475	0.29	0.3410	4.90	0.0521	4.91
9	299.2	0.3	299.5	3.0	302	26	0.08	0.98	59.7	3.3	18.3	1019	0.0475	0.11	0.3431	1.14	0.0524	1.14
10	298.9	0.3	299.5	3.5	304	31	0.04	1.63	48.2	3.2	15.3	859	0.0475	0.09	0.3431	1.36	0.0524	1.36
b-2	293.0	0.7	288.9	6.7	256	61	0.08	-14.5	58.2	7.7	7.57	459	0.0465	0.24	0.3292	2.65	0.0514	2.64
e) Standards																		
Standard 91500																		
91500–1	1059.6	2.7	1065.5	19.1	1064	53	0.96	0.38	13.4	3.5	3.81	258	0.1799	0.27	1.8558	2.90	0.0748	2.63
91500–2	1060.1	2.4	1054.3	16.1	1045	45	0.90	0.26	35.8	8.0	4.49	302	0.1785	0.25	1.8246	2.46	0.0741	2.23
91500–3	1061.1	2.0	1056.3	4.0	1047	11	0.58	1.35	76.7	7.0	11.0	697	0.1789	0.18	1.8300	0.61	0.0742	0.52
91500–4	1061.9	1.8	1062.4	11.8	1067	33	0.88	1.26	22.1	3.6	6.17	406	0.1788	0.19	1.8472	1.79	0.0749	1.63

Table 4 (continued)

Fraction and sample	Dates [Ma]								Composition			Isotopic Ratios						
	$^{206}Pb/^{238}U$	±2σ	$^{207}Pb/^{235}U$	±2σ	$^{207}Pb/^{206}Pb$	±2σ	Corr	%disc	Pb*	Pb_c	Pb*/Pb_c	$^{206}Pb/^{204}Pb$	$^{206}Pb/^{238}U$	±2σ	$^{207}Pb/^{235}U$	±2σ	$^{207}Pb/^{206}Pb$	±2σ
	a	(abs.)	a	(abs.)	a	(abs.)	Coeff	b	c	d	e	f	g	(%)	g	(%)	g	(%)
91500–5	1062.3	3.4	1060.6	23.6	1063	66	0.93	0.03	10.9	3.5	3.07	212	0.1787	0.35	1.8421	3.58	0.0748	3.26
91500–6	1063.0	2.1	1055.6	9.2	1042	26	0.66	2.26	77.3	9.4	8.19	537	0.1791	0.21	1.8281	1.40	0.0740	1.27
91500–7	1063.3	1.1	1063.8	6.9	1067	19	0.84	0.33	69.5	6.5	10.6	685	0.1791	0.12	1.8510	1.05	0.0749	0.95
91500–8	1063.5	1.4	1059.9	3.2	1056	9	0.66	3.26	59.6	6.1	9.71	632	0.1791	0.09	1.8402	0.48	0.0745	0.43
91500–9	1064.5	2.9	1059.2	3.5	1052	10	0.53	1.14	59.4	6.2	9.51	619	0.1792	0.15	1.8382	0.54	0.0744	0.48
91500–10	1064.6	2.9	1064.6	3.6	1072	10	0.58	4.26	55.4	7.8	7.06	464	0.1789	0.14	1.8533	0.54	0.0751	0.48
91500–11	1064.9	1.2	1064.9	5.2	1066	14	0.67	0.14	109	7.6	14.3	920	0.1795	0.13	1.8541	0.79	0.0749	0.71
91500–12	1065.3	1.2	1061.3	1.0	1055	2	0.86	5.26	278	7.7	36.2	2299	0.1795	0.08	1.8439	0.15	0.0745	0.09
91500–13	1065.8	2.4	1064.5	15.3	1064	42	0.87	0.16	57.2	12	4.74	318	0.1796	0.25	1.8529	2.31	0.0748	2.10
91500–14	1066.2	1.4	1064.9	6.4	1064	18	0.71	6.26	45.5	3.9	11.6	749	0.1797	0.14	1.8542	0.97	0.0749	0.87
91500–15	1067.6	2.9	1065.8	21.6	1065	60	0.97	0.24	41.4	12	3.37	231	0.1799	0.30	1.8567	3.27	0.0749	2.97
Standard Temora2																		
Tem-1	415.5	1.9	414.3	24.8	412	152	0.98	0.73	6.64	3.3	2.03	149	0.0664	0.49	0.5039	7.28	0.0550	6.80
Tem-2	416.5	1.9	416.7	3.1	419	17	0.55	0.64	185	9.9	18.6	1183	0.0667	0.40	0.5074	0.92	0.0552	0.78
Tem-3	416.8	0.9	418.3	11.0	429	67	0.93	2.86	15.6	3.4	4.55	302	0.0667	0.23	0.5098	3.20	0.0554	2.99
Tem-4	417.1	0.8	415.9	1.9	409	11	0.60	1.85	71.6	6.8	10.5	666	0.0668	0.10	0.5062	0.55	0.0549	0.49
Tem-5	417.2	0.6	417.9	5.9	423	36	0.86	1.48	32.8	3.8	8.66	562	0.0668	0.14	0.5091	1.74	0.0553	1.62
Tem-6	417.4	0.6	413.3	2.2	396	13	0.64	5.54	60.8	7.7	7.89	516	0.0667	0.09	0.5024	0.64	0.0546	0.59
Tem-7	417.8	0.7	414.3	2.1	401	13	0.65	4.09	62.6	11	5.96	400	0.0668	0.08	0.5038	0.63	0.0547	0.57
Tem-8	417.8	2.1	423.4	23.2	457	139	0.81	8.58	12.3	5.4	2.27	158	0.0669	0.58	0.5174	6.71	0.0561	6.25
Tem-9	418.2	0.9	418.6	6.3	423	38	0.76	1.03	31.3	5.9	5.32	350	0.0670	0.17	0.5102	1.83	0.0553	1.71
Tem-10	419.3	0.6	417.8	7.9	412	48	0.96	1.86	20.0	3.1	6.46	430	0.0671	0.16	0.5090	2.29	0.0550	2.14
Tem-11	419.7	1.9	417.5	18.8	409	115	0.83	2.65	12.6	4.6	2.76	192	0.0672	0.45	0.5086	5.49	0.0549	5.13
Tem-12	425.3	0.9	422.0	11.0	407	67	0.92	4.60	15.8	3.4	4.67	317	0.0681	0.23	0.5153	3.19	0.0549	2.97
Tem-13	429.5	1.8	422.2	22.8	388	139	0.96	10.8	8.40	3.7	2.24	162	0.0687	0.45	0.5156	6.61	0.0544	6.18

[a]Isotopic dates calculated using $\lambda_{238} = 1.55125E\text{-}10$ (Jaffey et al. 1971) and $\lambda_{235} = 9.8485E\text{-}10$ (Jaffey et al. 1971)

[b]% discordance = 100—(100 * ($^{206}Pb/^{238}U$ date) / ($^{207}Pb/^{206}Pb$ date))

[c]Total mass of radiogenic Pb

[d]Total mass of common Pb

[e]Ratio of radiogenic Pb (including ^{208}Pb) to common Pb

[f]Measured ratio corrected for fractionation and spike contribution only

[g]Measured ratios corrected for fractionation, tracer and blank

highlighted samples were used for $^{206}Pb/^{238}U$ mean age calculation

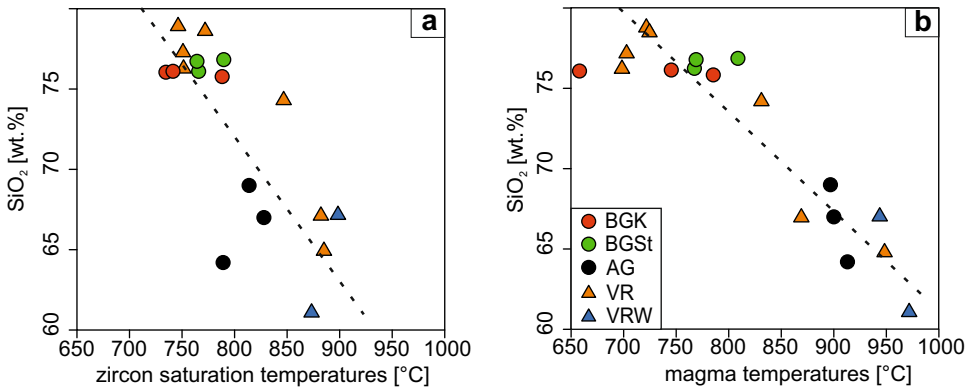

Fig. 6 Zircon saturation temperatures (**a**) calculated according to **a** Watson and Harrison (1983) and magma temperatures (**b**) calculated according to Jung and Pfänder (2007) vs. SiO_2 content of the whole-rock samples. The sample groups are *BGK* biotite-bearing granite of the Koenigshain pluton, *AG* amphibole nearing granite, *BGSt* biotite-bearing granite of the Stolpen pluton, *VR* volcanic rocks in dykes, *VRW* volcanic rocks within the Weissig basin

zircons from each group of samples (except for amphibole-bearing granites) and Pb–Pb evaporation data of single zircons. Based on these data, we selected samples for additional CA–ID–TIMS and SHRIMP dating. Samples with zircons frequently showing Pb loss and/or elevated Pb_c, and/or inherited ages were excluded from further CA–ID–TIMS dating (Fig. 7). Detailed results of Pb–Pb evaporation analysis are tabulated in Supplement 1.

Zircons of the biotite-bearing granites of the Koenigshain pluton show oscillatory zoning in their interior zones covered by broad black CL rims (Fig. 7a). These zircons contain inclusions of apatite, biotite, and muscovite and, less frequently, quartz, feldspar, and ilmenite. The zircons show dominance in {101} pyramids and some variation in prims from {110} to {100} (Hammer 1996). Zircon Pb–Pb evaporation dating yielded similar mean ages for all four samples from Koenigshain with only very few younger grains (interpreted as Pb loss) and few older, inherited grains. The calculated mean intrusion ages of the four samples from Koenigshain vary from 319 ± 7 Ma to 324 ± 4 Ma (Fig. 7). Despite some single grains with elevated Pb_c ($^{204}Pb/^{206}Pb > 0.0002$), all four Koenigshain samples seem equally suitable for zircon U–Pb CA–ID–TIMS and SHRIMP dating. The sample BGK1 was chosen for additional SHRIMP and CA–ID–TIMS dating, and sample BGK4 was chosen in addition for CA–ID–TIMS dating to obtain ages from the two small plutons separated by the granodioritic Cadomian basement and a fault (Fig. 2c).

Zircons of the biotite-bearing granites of the Stolpen pluton display oscillatory zoning, similar to those of the biotite-bearing rocks of the Koenigshain pluton (Fig. 7b), but without broad black CL rims. Frequent inclusions are biotite, apatite, quartz, and feldspar. Similar to the biotite-bearing granites of the Koenigshain pluton, zircons show dominance in {101} pyramides and {100} as well as {110} prisms (Hammer 1996). Zircon Pb-Pb evaporation data of these samples revealed minor Pb loss and only few inherited ages. The calculated mean ages of the three samples vary from 304 ± 2 Ma to 308 ± 5 Ma and are therefore significantly younger than the samples from the Koenigshain pluton (Fig. 7b). BGSt11 and BGST14 were chosen for additional CA-ID-TIMS-dating.

Amphibole-bearing granitoids can be distinguished from the biotite-bearing granites by their zircon morphology showing co-existence of {100} prisms and {211} pyramids (Hammer 1996). In zircon Pb–Pb evaporation data, no Pb loss was detected but a significant portion of inherited ages was obtained that often were only slightly older than the calculated intrusion ages (from 322 ± 5 to 325 ± 5 Ma). Sample AG61 was selected for CA-ID-TIMS dating because the inherited ages are much older compared to the intrusion ages and therefore can easily be distinguished, while Pb_c contents in most grains were low (Fig. 7c).

Zircons from volcanic dykes share the morphology and internal structure of both biotite-bearing granitic plutons. Inclusions in zircons are smaller than those in the biotite-bearing granites and have been identified as apatite, biotite, quartz, feldspar, and ilmenite. The zircon evaporation data scatter over a wide range with calculated weighted mean ages from 296 ± 6 to 326 ± 3 Ma. Most of the samples display both inheritance and Pb loss (Fig. 7d). Elevated Pb_c rarely occurs in zircons of most volcanic dykes. None of the volcanic dyke samples was dated with zircon U–Pb CA–ID–TIMS.

Although zircon characteristics of the volcanic rocks of the Weissig basin do not differ from volcanic dykes, slight rounding of zircon grains can be recognized, particularly in sample VRW67 from the Hutberg Formation of the Weissig basin (Fig. 7e). The weighted mean ages for samples VRW65 and VRW67 are 306 ± 4 Ma and 304 ± 4 Ma,

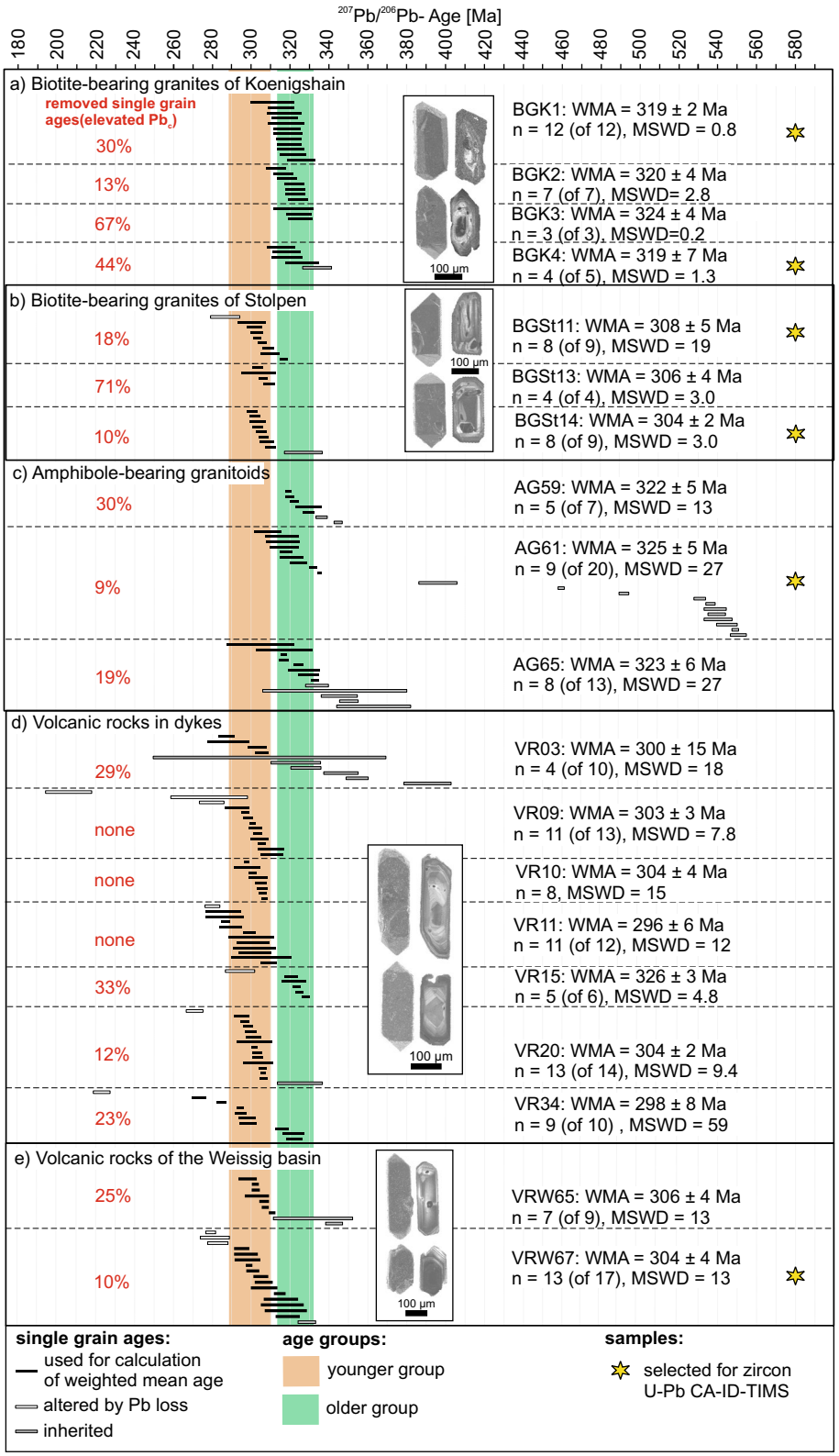

Fig. 7 Summary of zircon Pb–Pb evaporation data that were used as screening to select samples that are best suited for high-precision zircon U–Pb CA–ID–TIMS dating. Selected samples should have zircons with low amounts of inherited grains, low amounts of common Pb ($^{204}Pb/^{206}Pb \leq 0.0002$), and low degree of Pb loss. Grains with $^{204}Pb/^{206}Pb > 0.0002$ were discarded and are not presented in the Tables (Supplement 1) and in this Figure. For each sample, the left column (red text) gives the amount of single-grain ages (in %) that have been removed from the dataset because of elevated common Pb ($^{204}Pb/^{206}Pb > 0.0002$). Representative CL images are given for each sample group, if available. Weighted mean ages were calculated with Isoplot/Ex (Ludwig 2008). Uncertainties on mean ages are 95%-confidence errors. The zircon Pb-Pb evaporation data define two groups of crystallization ages, marked as coloured bands

respectively. Single grain zircon Pb–Pb evaporation ages reveal inheritance in both samples of the Weissig basin and additional Pb loss in sample VWR67. Nevertheless, this sample was chosen for zircon U–Pb CA–ID–TIMS dating because it contains few inherited grains and few grains with elevated Pb_c.

From the new zircon evaporation age data, the biotite and amphibole-bearing granitic rocks of the northern

Lusatian Block can be subdivided into two well-defined groups (Fig. 7). The older group comprises the biotite-bearing granites of the Koenigshain pluton (mean ages from 319 ± 7 to 324 ± 4 Ma), the amphibole-bearing granites (mean ages from 322 ± 5 to 325 ± 5 Ma), and probably one volcanic dyke (VR15, mean age of 326 ± 3 Ma). The younger group comprises the biotite-bearing Stolpen granites (from 304 ± 2 to 308 ± 5 Ma), six out of seven volcanic dykes (VR03, VR15, VR20, VR28, VR34, from 296 ± 6 to 304 ± 4 Ma), and probably the volcanic rocks from the Weissig basin (from 304 ± 4 to 306 ± 4 Ma, although several single measurements yielded ages up to 320 Ma).

Zircon U–Pb age determinations by SHRIMP

Sample BGK1 was dated using the zircon U–Pb SHRIMP method. The results of these analyses are given in Table 3 and Supplement 2. The single measurements range from 321 ± 4 to 327 ± 3 Ma (Table 3). A Concordia age of 323.9 ± 2.1 Ma (MSWD of concordance = 0.42) was calculated from all eleven spot analyses (Figure in Supplement 2). This age is ca. 4 Ma older than the zircon Pb-Pb evaporation date of this sample (319 ± 2 Ma) although both ages overlap within errors.

Zircon U–Pb age determinations by CA–ID–TIMS

Zircon U–Pb CA–ID–TIMS isotopic results for six samples are presented in Table 4 and shown as $^{206}Pb/^{238}U$ ranked age plots in Fig. 8. For each sample, 10–23 grains were analysed by this method. Mean sample ages representing the crystallization event were calculated from established age clusters with the software ET_Redux (Bowring et al. 2011). The error includes the internal 2σ measurement error, the tracer calibration uncertainty, and the uncertainty of the decay constant, allowing for a comparison with ages determined by different dating methods (Schoene et al. 2006: z error).

Analysis of 14 zircons from sample BGK1 yielded ages between 308.6 ± 0.7 Ma and 316.2 ± 1.2 Ma (Fig. 8, Table 4). Four zircons yielded identical ages resulting in a mean age of 312.7 ± 0.4 Ma ($n = 4$) which is interpreted as the intrusion age. Older ages are supposed to be zircons incorporated during intrusion from slightly older magma batches (antecrystic grains, Miller et al. 2007). Single ages that are younger than the cluster used for mean age calculation are interpreted as slight Pb loss.

A second sample (BGK4) was dated from the same pluton. The first attempt to date this sample (17 zircons, analysis numbers 1–12 and14–18 in Table 4) revealed variable ages from 302.4 ± 0.4 to 316.0 ± 0.5 Ma. We interpreted the large age scatter towards younger ages as Pb loss. For this

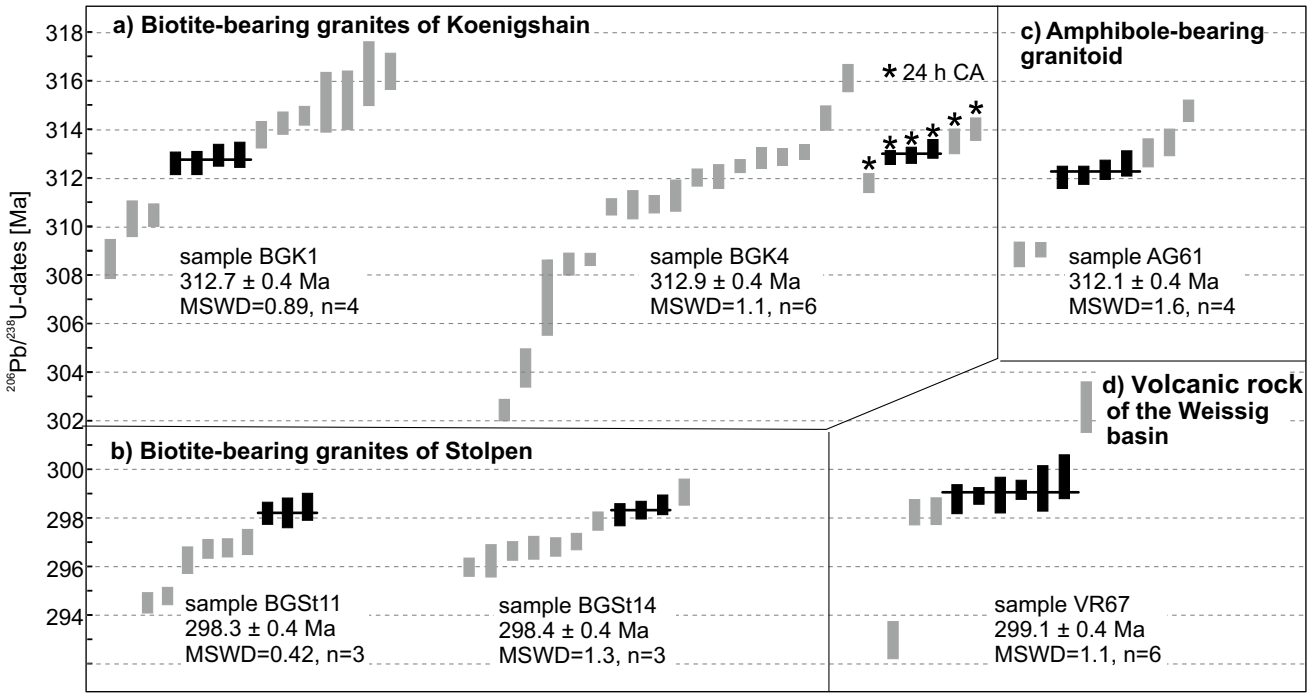

Fig. 8 Single grain zircon U–Pb CA–ID–TIMS analyses as $^{206}Pb/^{238}U$ weighted mean dates for granitic and volcanic samples, calculated with the software ET_Redux (Bowring et al. 2011). Each vertical bar represents a single zircon grain analysis including its 2σ analytical (internal) uncertainties whereas data represented by grey bars are not included in the weighted mean calculation. Horizontal black lines represent the weighted mean age

reason, we applied an additional leaching procedure to the remaining zircons (24 instead of 12 h, analysis number b-1 to b-6 in Table 4). The single ages from zircons leached 24 h show less scatter (from 311.2 ± 0.6 to 313.9 ± 0.4 Ma) and support our suggestion of Pb loss for the youngest single dates. An age cluster at 312.9 ± 0.4 Ma ($n = 3$) is interpreted as the intrusion age of this sample from three zircon ages with 24 h leaching (Fig. 8a). From this data set, two single-grain ages are up to 1 Ma older than this cluster and are interpreted as antecrystic grains. Within error, the intrusion ages of both samples from the Koenigshain granite are equal (312.7 ± 0.4 and 312.9 ± 0.4 Ma).

Two samples were dated from the biotite-bearing granite of Stolpen. Two out of 11 single-grain ages of sample BGSt11 are obviously (~ 20 Ma) older than the main age cluster (Table 4, 318.2 ± 0.9 Ma, 323.3 ± 0.8 Ma). From the remaining 9 single-grain dates (ranging from 294.5 ± 0.3 to 298.5 ± 0.5 Ma), the oldest dates are concordant and form a cluster, while younger ages are slightly (but increasingly) discordant (Supplement 3). Thus, we interpret the oldest group as the intrusion age of this sample (Fig. 8b, 298.3 ± 0.4 Ma, $n = 3$). Based on their discordancy, the slightly younger ages (up to 4 Ma) are interpreted to result from Pb loss (e.g., Mezger and Krogstad 1997; Schoene 2014).

All age data of sample BGSt14 cluster between 295.3 ± 2.1 Ma and 299.1 ± 0.4 Ma (Fig. 8, Table 4). As in sample BGSt11, the Concordia diagram displays discordant pattern for younger ages (< 298 Ma, Supplement 3). Consequently, we used the oldest age cluster for the calculation of the intrusion age (298.4 ± 0.4 Ma, $n = 3$). One single slightly older age (299.1 ± 0.4 Ma) is interpreted as antecrystic zircon. The resulting mean ages of both samples from the Stolpen granite are therefore identical within error (298.3 ± 0.4 and 298.4 ± 0.4 Ma).

Five out of 16 single-grain analyses from the amphibole-bearing granite (sample AG61) yielded much older ages than the remaining dates (Table 4, 356 ± 2 to 537.7 ± 0.3 Ma). We interpret these data as inherited grains. Two distinctly younger dates at ca. 309 Ma are interpreted as Pb loss. The remaining seven single-grain ages define a cluster with a weighted mean age of 312.1 ± 0.4 Ma ($n = 4$, Fig. 8). A tail towards older ages is interpreted as antecrystic zircon grains or mixed ages.

From the volcanic rock from the Weissig basin (sample VRW67) ten single zircon grains were analysed. Besides one antecrystic grain (302.6 ± 1.0 Ma) and slight Pb loss in three grains, an age cluster from six analyses yielded a weighted mean age at 299.1 ± 0.4 Ma. This age is interpreted as the eruption age of this volcanite (Fig. 8, Table 4).

Whole-rock Nd- and Sr-isotope ratios

Nd- and Sr-isotopes were determined for the four biotite-bearing granites of Koenigshain (samples BGK1, BGK2, BGK3, BGK4) and are listed in Table 5. The εNd values of these samples range from − 4.2 to − 0.8 ($t = 320$ Ma) with two-stage model ages according to Liew and Hofmann (1988) ranging from 1.1 to 1.4 Ga.

Zircon geochemistry: Hf- and O-isotope ratios

The measured zircons from sample BGK1 have relatively uniform Hf and very homogeneous O-isotopic compositions (Table 6, Supplement 4). The hafnium isotope ratio $^{176}Hf/^{177}Hf$ varies from 0.282472–0.282576 (corresponding to εHf(t) = − 0.6 to − 4.1 ($t = 320$ Ma)), and the oxygen isotope value ($\delta^{18}O$) varies from 6.0 to 6.8‰. Hf model ages range from 1.2 to 1.4 Ga that are identical with the zircon Nd model ages.

Discussion

Comparison of zircon ages analysed with different U–Pb methods (evaporation, SHRIMP, TIMS)

The Pb–Pb zircon evaporation data of biotite and amphibole-bearing granites acquired during this study are systematically older than the ages determined for the same samples with the zircon U–Pb CA–ID–TIMS method (Fig. 9). The offset in ages varies between 1.3 and 4.1% and the error bars do not overlap with the CA–ID–TIMS ages (Fig. 9). This systematical bias of the evaporation data can best be explained by the ca. 1% older age of the secondary standard Temora in comparison to the values published by Black et al. (2004, Supplement 4) and the relatively young Phanerozoic ages of our samples. Generally, Phanerozoic $^{207}Pb/^{206}Pb$

Table 5 Sm–Nd isotope data

Sample	Sm ppm	Nd ppm	$^{147}Sm/^{144}Nd$	$^{143}Nd/^{144}Nd$	2 SE	εNd (312 Ma)	TDM (Ma)[1]
BGK1	6.6	23.8	0.1767	0.512379	2	− 4.24	1.370
BGK2	6.8	22.7	0.1811	0.512567	4	− 0.75	1.096
BGK3	6.6	17.9	0.2229	0.512523	5	− 3.32	1.297
BGK4	6.4	30.7	0.1260	0.512347	12	− 2.79	1.256

1: two-stage model age according to Liew and Hofmann (1988)

Table 6 LA–MC–ICP–MS Lu–Hf isotope data and SIMS oxygen isotope data of zircons from sample BGK1

zrn-spot	$^{176}Yb/^{177}Hf$[a]	±2σ ±0.00xx	$^{176}Lu/^{177}Hf$[a]	±2σ ±0.000xx	$^{176}Hf/^{177}Hf$	±2σ[b] ±0.0000xx	$^{176}Hf/^{177}Hf_{(t)}$[c] (t = 320 Ma)	$eHf_{(t)}$[c] (t = 320 Ma)	±2σ[b]	T_{NC}[d] (Ga)	$d^{18}O$ (‰)	1SD	$^{206}Pb/^{238}U$ age*
3-a	0.0373	56	0.00121	13	0.282553	22	0.282546	− 1.3	0.8	1.23	6.0	0.3	326.9
5-a	0.0213	17	0.00082	5	0.282472	17	0.282467	− 4.1	0.6	1.38	6.8	0.3	325.9
8-a	0.0244	24	0.00082	6	0.282518	22	0.282513	− 2.5	0.8	1.29	6.4	0.3	326.8
10-a	0.0751	83	0.00221	21	0.282539	21	0.282526	− 2.0	0.8	1.27	6.3	0.3	323.0
11-a	0.0374	35	0.00127	10	0.282556	25	0.282549	− 1.2	0.9	1.22	6.6	0.3	322.6
12-a	0.0396	32	0.00136	8	0.282576	19	0.282568	− 0.6	0.7	1.19	6.2	0.3	322.9
13-a	0.0331	29	0.00114	7	0.282504	20	0.282497	− 3.1	0.7	1.32	6.3	0.3	322.6
14-a	0.0458	53	0.00152	14	0.282575	27	0.282566	− 0.6	1.0	1.19	6.7	0.3	320.8
15-a	0.0179	15	0.00062	4	0.282541	21	0.282538	− 1.6	0.7	1.25	6.4	0.3	321.1

[a] $^{176}Yb/^{177}Hf = (^{176}Yb/^{173}Yb)true \times (^{173}Yb/^{177}Hf)meas \times (M^{173}(Yb)/M^{177}(Hf))b(Hf)$, $b(Hf) = \ln(^{179}Hf/^{177}Hf_{true} / {}^{179}Hf/^{177}Hf_{measured}) / \ln(M^{179}(Hf)/M^{177}(Hf))$, M = mass of respective isotope

The $^{176}Lu/^{177}Hf$ were calculated in a similar way using the $^{175}Lu/^{177}Hf$ and b(Yb)

[b] Uncertainties are quadratic additions of the within-run precision and the daily reproducibility of the 40 ppb-JMC475 solution. Uncertainties for the JMC475 quoted at 2SD (2 standard deviation)

[c] Initial $^{176}Hf/^{177}Hf$ and eHf calculated using the apparent Pb-Pb age determined by LA–ICP–MS dating (= 320 Ma), and the CHUR parameters:

$^{176}Lu/^{177}Hf = 0.0336$, and $^{176}Hf/^{177}Hf = 0.282785$ (Bouvier et al., 2008)

[d] two stage model age in billion years using the measured $^{176}Lu/^{177}Lu$ of each spot (first stage = age of zircon), a value of 0.0113 for the average continental crust (second stage), and a juvenile crust (NC)

* SHRIMP spot age according to Table 3

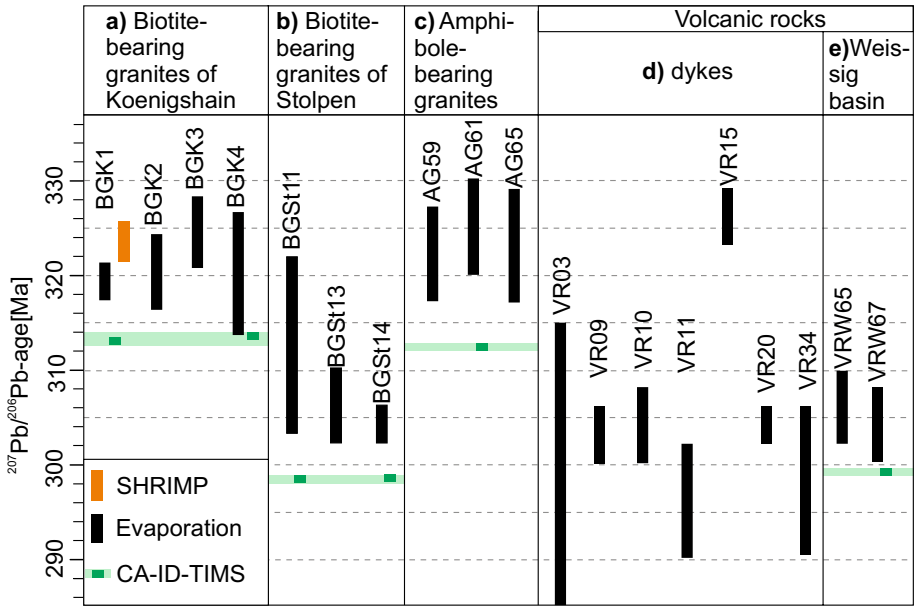

Fig. 9 Summary of new zircon data acquired with different methods. Mean $^{207}Pb/^{206}Pb$ ages from zircon evaporation are shown as vertical black bars. One weighted mean $^{206}Pb/^{238}U$ SHRIMP age is shown as a vertical orange bar. Mean $^{206}Pb/^{238}U$ CA–ID–TIMS ages are shown as vertical dark green bars. Light green bars represent the variation range of all $^{206}Pb/^{238}U$ CA–ID–TIMS sample ages for a certain rock group (e.g. group **a**, **b**, **c**, and **e**)

ages are less reliable in comparison to Precambrian ages, because for ages < 1 Ga, the difference of $^{207}Pb/^{206}Pb$ ratios strongly decreases towards younger ages.

The SHRIMP age of sample BGK1 is with 323.9 ± 2.1 Ma ca. 3.7% older than the CA–ID–TIMS age (312.2 ± 0.4 Ma, Fig. 9). The accuracy of our SHRIMP age cannot be assessed, because it was determined without the parallel measurement of a secondary standard in 2011. Thus, the uncertainty is only a statistical error, excluding external components. The absolute age resolution of SHRIMP has been estimated as 1–2% (Schaltegger et al., 2015). However, even with an uncertainty of 2%, the SHRIMP age is still significantly older than the CA–ID–TIMS age. Tichomirowa et al. (2019a) compared CA–ID–TIMS with SHRIMP ages from the same samples of Variscan granites from the Western Erzgebirge. While single SHRIMP ages based on ca. 10 measurement have shown similar deviations from CA–ID–TIMS ages, the mean of several samples from the same pluton (corresponding to > 30 data points) resulted in a SHRIMP age identical with CA–ID–TIMS data. Therefore, we suggest that the small number of single data points for BGK1 sample ($n = 11$) may explain the deviation to the CA–ID–TIMS age.

Two-phase igneous activity on the Lusatian Block

Our new CA–ID–TIMS data of Variscan post-collisional granitoids and volcanics of the Lusatian Block indicate two short episodes (1–2 Myr) of magmatic activity (Fig. 8). The older magmatic event records the intrusion of the Koenigshain granites and the amphibole-bearing granitoids and is restricted to 312–313 Ma. The younger magmatic event (the formation of the Stolpen granite and the volcanic rocks of the Weissig basin) occurred between 298 and 299 Ma.

Despite being shifted towards older ages, our Pb-Pb evaporation data in general support the conclusion that Variscan igneous activity on the Lusatian Block occurred in two separate events (Fig. 7). However, some of the evaporation ages overlap due to large errors and cannot clearly be assigned to the younger or older group, respectively (Figs. 7, 9: BGK 4, BGST11, VR03). Nonetheless, taking both CA-ID-TIMS and evaporation data into consideration, the Koenigshain granite, the amphibole-bearing granite and one of the dykes (VR15) can be assigned to the older group. The younger group is represented by the Stolpen granite, most of the dykes, as well as volcanites from the Weissig basin (Fig. 9).

From the Koenigshain pluton, three main granite varieties are described (porphyritic granite, equigranular leucogranite, and fine-grined monzogranite) that are geochemically different and sometimes show internal intrusion contacts (Eidam and Götze 1991; Hecht et al. 1999). The porphyritic (BGK4) and the equigranular varieties (BGK1) yielded within errors identical ages (312.7 ± 0.4 Ma; 312.9 ± 0.4 Ma). Similarly, the two main granite facies (porphyritic and equigranular granites) of the Karkonosze pluton gave indistinguishable zircon U–Pb CA–ID–TIMS ages at ca. 312 Ma (Kryza et al. 2014b). According to these data, the Koenigshain pluton and the Karkonosze pluton belong to the same magmatic event. These results are in line with further high-precision CA–ID–TIMS ages that record intrusion activity of some large composite plutons—composed of several magma batches—within ca. 2 Myr (e.g., Kryza et al. 2014b; Ratschbacher et al. 2018; Tichomirowa et al. 2019a).

Both the 298–299 Ma and the 312–313 Ma magmatic events of the Lustian Block were probably accompanied

by the intrusion of subvolcanic rocks as dykes. Field relationships, like, e.g. dykes that crosscut the granitic rocks (Kozdrój et al. 2001, Fig. 2b, c), suggest that some of the dykes may be younger than the granitic rocks.

In the Weissig basin, biostratigraphic correlations to other, chronostratigraphically well-defined basins can provide insight into the age of volcanic rocks interlayered with fossil-bearing sediments and help to assess age data. Fossil macroflora of the Weissig basin suggests that the Hutberg Formation is possibly older than the Napoleonstein Formation (Barthel et al. 2010; Reichel 2012; Fig. 3). A stratigraphic relationship of the two formations cannot be determined, because they occur in different parts of the Weissig basin. A correlation of the Hutberg Formation with the *Acanthodes* horizon of the Goldlauter Formation of the Thuringian Forest (Reichel 2012) indicates an age between 296.9 ± 0.4 and 299.3 ± 0.3 Ma (zircon U–Pb CA–ID–TIMS data of igneous rocks in the Thuringian Forest, Lützner et al. 2021). Our new CA–ID–TIMS age of the Napoleonstein Formation (299.1 ± 0.4 Ma; Fig. 8) well corresponds to this time interval for the *Acanthodes* horizon and may serve as an argument for the nearly contemporaneous formation of the Hutberg and Napoleonstein units of the Weissig basin. All volcanic rocks of the Weissig basin can thus be assigned to the younger magmatic episode (Fig. 9).

Identification of sources for amphibolite-bearing and biotite-bearing granites

In the literature, the subdivision of the Lusatian Variscan igneous rocks into amphibole-bearing and biotite-bearing granitoids in Germany is consensus (e.g., Eidam et al. 1995; Hammer 1996; Hecht et al. 1999; Hammer et al. 1999; Lisowiec et al. 2013, 2014). While biotite-bearing granites exist in both age groups (312–313 Ma for Koenighshain and 298–299 Ma for Stolpen), all dated amphibole-bearing rocks belong to the older group. In addition to their distinct petrographic composition, amphibole- and biotite-bearing rocks have a different whole-rock geochemistry (Figs. 4, 5, Table 2) as well as Sr- and O-isotope composition (Hammer 1996; Hammer et al. 1999), and zircon morphology (Hammer 1996). Our new Nd-isotopic data of samples BGK1, BGK2, BGK3, and BGK4 from the biotite-bearing granites of Koenigshain overlap with those of the amphibole-bearing granitoid data from Hammer (1996) and do not confirm a difference in Nd-isotopic ratio of both rock types (Hammer 1996). However, calculated magma temperatures are higher for amphibole-bearing granites compared to biotite-bearing granites (Fig. 6). Probably, the biotite- and amphibole-bearing granites have different sources.

Hammer (1996) and Hammer et al. (1999) concluded that tholeiitic rocks are the most suitable and dominant source for amphibole-bearing granitoids. The enrichment of LILE and HFSE elements was explained by these authors as being caused by a subduction-induced metasomatic overprint of a mafic source.

The probable source of biotite-bearing granites is less well defined. Hammer (1996) and Hammer et al. (1999) proposed another dominant, probably metapelitic source for these granites. This assumption is based on a comparison with whole-rock geochemical data of the Variscan Eisgarn granite of Austria, which is thought to have a metapelitic educt (Vellmer and Wedepohl 1994). Hammer (1996) also documented enrichment in LILE and HFSE in the biotite-bearing granites and interpreted this as a supply of elements and volatiles during partial melting instead of source enrichment.

Isotope data on zircon are particularly suitable to determine sources of rocks, because these data are not affected by fractional crystallization or hydrothermal overprint and thus represent the composition of the melt (Chen and Zheng 2017; Tichomirowa et al. 2019b). The zircon Hf data from sample BGK1 (biotite-bearing granite of Koenigshain, Table 6) vary from $\varepsilon Hf_{(t)} = -4.1$ to nearly chondritic ratios ($\varepsilon Hf_{(t)} = -0.6$). In addition, zircon $\delta^{18}O$ values (6.0–6.7‰) are very homogeneous but slightly higher than pure mantle values (5.3 ± 0.3‰, Valley et al. 2005). The calculated $\delta^{18}O$ values of the corresponding melts (8.2—8.9‰, Lackey et al. 2008) agree with the analysed whole-rock $\delta^{18}O$ values of these biotite-bearing granites (Hammer 1996, $\delta^{18}O$ from 8.3 to 9.2‰). Accordingly, the Lusatian biotite-bearing granites can be classified as I-type granites (Chappell and White 2001). A dominant sedimentary source for the biotite-bearing granites ($\delta^{18}O$ typically 10–30‰, Valley et al. 2005) can be excluded, so that a metapelitic source rock—as suggested by Hammer (1996) and Hammer et al. (1999)—is implausible. Intermediate to acidic igneous rocks ($\delta^{18}O$ typically 5–10‰, Valley et al. 2005) are the most likely sources for the biotite-bearing granites from Koenigshain.

A direct comparison of zircon Hf and $\delta^{18}O$ values of sample BGK1 with potential source rocks is limited by the small amount of published Hf- and O-isotope data from the Lusatian Block. A comparison with other Cadomian basement rocks and Variscan igneous rocks of the Saxothuringian Zone reveals the difference of Hf and $\delta^{18}O$ values for sample BGK1 (Fig. 11). Both the Variscan igneous rocks of the North German basin and of the Polish lowlands show distinctly higher $\delta^{18}O$ values and mostly lower but scattering εHf (Pietranik et al. 2013; Słodczyk et al. 2018) indicating distinct sources. The Variscan granites of the Western Erzgebirge show similarly homogeneous εHf but slightly higher $\delta^{18}O$ values compared to zircons from sample BGK1 (Tichomirowa et al. 2019b, Fig. 10). Variscan high-grade metamorphic amphibolite facies and granulite-facies gneisses (metamorphism between 360 and 330 Ma, e.g., Schmädicke et al. 1995; Kröner and Willner 1998;

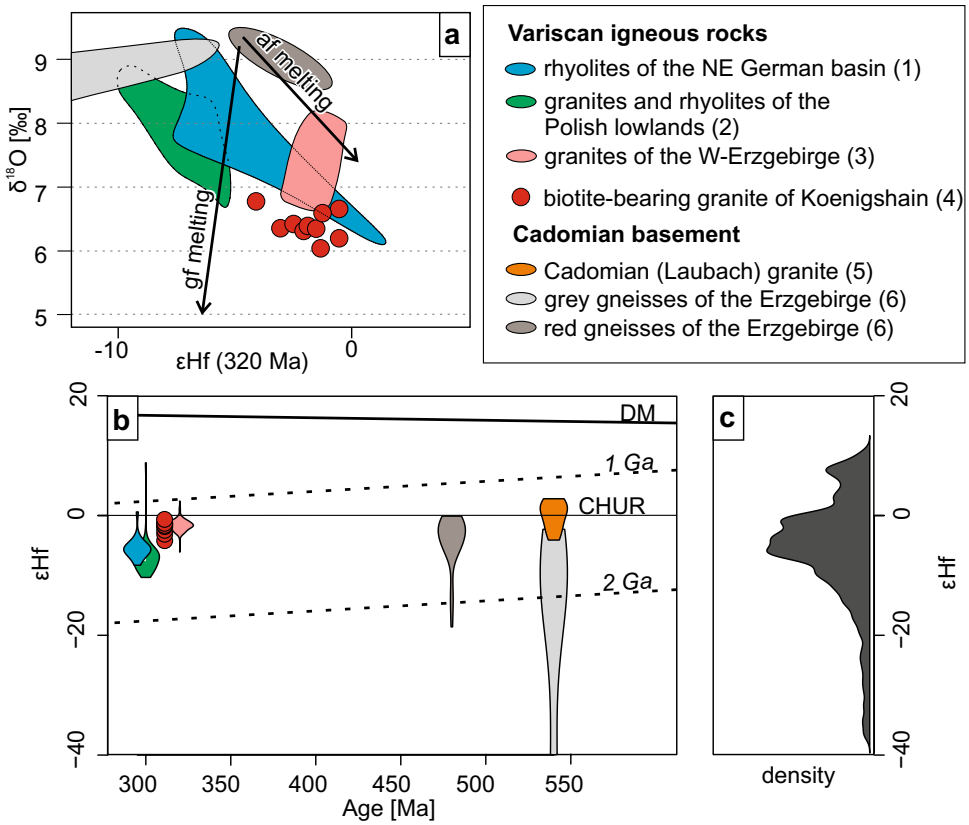

Fig. 10 Summary of zircon Hf and O data. Data are from: 1—Pietranik et al. (2013), 2—Słodczyk et al. (2018), 3—Tichomirowa et al. (2019b), 4—this study, 5—Linnemann et al. (2014), 6—Tichomirowa et al. (2018). a) εHf (320 Ma) versus $\delta^{18}O$ values from the same spot locations within zircons from sample BGK1 (Koenigshain pluton) in comparison with data from Variscan gneisses and granites of the Erzgebirge, NE German basin, and Polish lowlands. Abbreviations are af-melting—amphibolite-facies melting, gf-melting—granulite-facies melting according to Tichomirowa et al. (2018) b) Hf-isotope evolution diagram with εHf-data as violin plots (i.e., mirrored probability density plots according to Hintze and Nelson, 1998). CHUR = chondritic uniform reservoir; DM = depleted mantle. **c** Vertical probability density function of Cadomian sediments of the Schwarzburg antiform (ages between 0.5 and 3.5 Ga, data from Linnemann et al. 2014)

Tichomirowa et al. 2005) have been proposed as the most likely source for these Variscan granites from the Western Erzgebirge based on their zircon data (Hf- and O-isotopes, xenocrystic ages) and their homogeneous model ages (Hf, Nd: 1.3–1.2 Ga, Tichomirowa et la. 2019b). A homogenization of the Hf-isotopic composition in zircon requires an almost complete dissolution of inherited zircons (Farina et al. 2014). However, inherited zircons are abundant in all Cadomian basement rocks of the Bohemian Massif (e.g., Tichomirowa et al. 2001, 2012; Tichomirowa 2002; Friedl et al. 2004; Białek et al. 2014; Zieger et al. 2018). In addition to frequent inherited zircons, all rocks from the Cadomian basement have very heterogeneous zircon Hf- and O-isotope composition as shown for the Saxothuringian basement of the Erzgebirge (Tichomirowa et al. 2018) and of the Schwarzburg Antiform (Linnemann et al. 2014). The almost non-metamorphosed Cadomian basement of the Lusatian Block is composed of the same Cadomian basement as in the Erzgebirge. Therefore, the basement rocks in both the Lusatian Block and the Erzgebirge share many similarities (bulk rock composition, zircon morphology, abundance and ages of inherited zircons, Tichomirowa et al. 2001, 2012), although in the Erzgebirge, the rocks later underwent a high-grade Variscan metamorphism. The Hf and Nd model ages of the biotite-bearing Koenigshain granite (sample BGK1) are very homogeneous (ca. 1.3–1.2 Ga, Fig. 10b), excluding exposed Cadomian basement rocks (that usually have model ages > 1.5 Ga, Tichomirowa et al. 2012) as dominant source rocks (Fig. 10a). Consistent with the homogeneous Hf-isotopic composition, the number of randomly dated inherited grains in the biotite-bearing granites was very small in both evaporation and CA-ID-TIMS dating (< 5%; Table 4, Supplement 1).

In summary, we agree with the supposed dominant mantle source (tholeiites) for the amphibole-bearing granitoids (Hammer 1996; Hammer et al. 1999). Biotite-bearing granites probably had a different source. Based on our

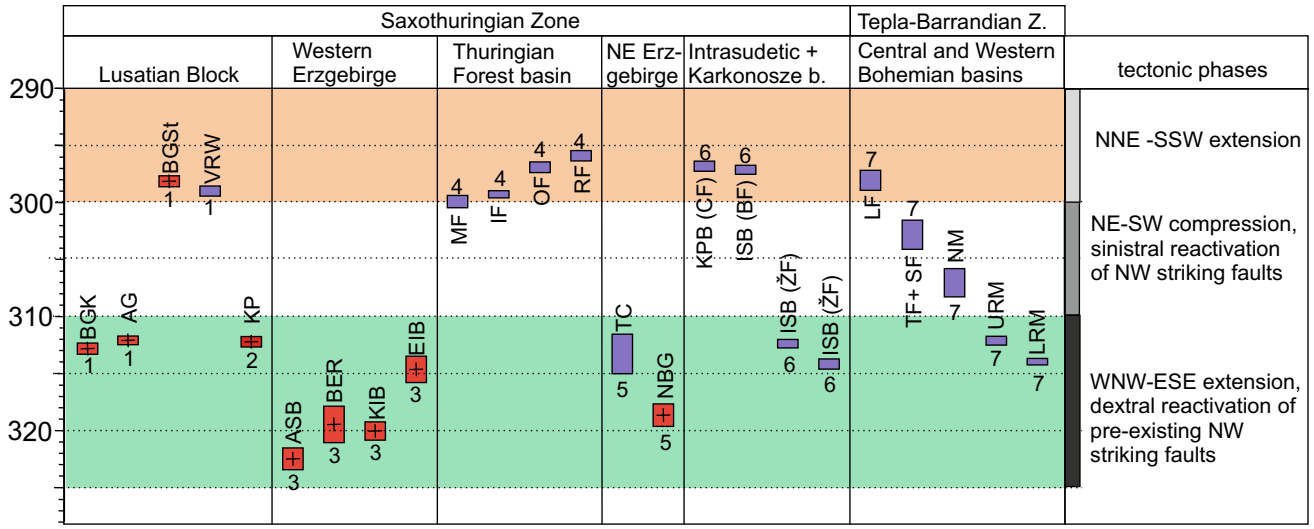

Fig. 11 Compilation of CA–ID–TIMS ages of Variscan magmatic rocks of the Saxothuringian Zone and of the adjoining Tepla-Barrandean volcano-sedimentary basins. Tectonic phases have been adopted from Edel et al. (2018) and Mazur et al. (2020). Age data are from 1—this study, 2– Kryza et al. 2014b, 3—Tichomirowa et al. (2019a), 4—Lützner et al. (2021), 5—Breitkreuz et al. (2021), 6—Opluštil et al. (2016a), 7—Opluštil et al. (2016b). Red colours represent granitic plutons, purple colours represent volcanic rocks. *BGK*—biotite-bearing granitoids of the Koenigshain pluton, *AG* –amphibole-bearing granitoids, *BGSt* biotite-bearing granites of the Stolpen pluton, *VRW* volcanic rocks of the Weissig basin, *KP* Karkonosze pluton, *ASB* Aue-Schwarzenberg pluton, *BER* Bergen pluton, *KIB* Kirchberg pluton, *EIB* Eibenstock pluton, *MF* Möhrenbach Formation, *IF* Ilmenau Formation, *OF* Oberhof Formation, *RF* Rotterode Formation, *TC* Tharandt Caldera, *NBG* Niederbobritzsch pluton, *KPB* Karkonosze piedmont basin, *ISB* Intra-Sudetic basin, *CF* Chotěvice Formation, *BF* Broumov Formation, *ŽF* Žacler Formation, *LF* Líně Formation, *TF* Týnek Formation, *SF* Slaný Formation, *NM* Nýřany Member, *URM* Upper Radnice Member, *LRM* Lower Radnice Member. As for the Lusatian Block an older and a younger magmatic phase were defined for the Saxothuringian Zone from these data and are marked with a green and an orange bar, respectively

Hf- and O-isotopes in zircon, we can exclude a dominant metapelitic source as suggested by Hammer (1996) and Hammer et al. (1999). The homogeneity of these isotopes also excludes most of the exposed Saxothuringian (Erzgebirge or Lusatian) basement rocks as one of the dominant sources. Intermediate to acidic igneous rocks of unknown ages seem to be the most likely source for the Variscan biotite-bearing granites. The old model ages require a contribution from old (subducted) crust, while their low zircon $\delta^{18}O$, relatively high Hf- and Nd-isotope compositions indicate an additional input from a mantle source. In comparison to other basement rocks of Saxothuringia (Pietranik et al. 2013; Linnemann et al., 2014; Słodczyk et al. 2018; Tichomirowa et al. 2018, 2019b; Fig. 10b), the Hf- and Nd-isotope compositions are higher and Hf and Nd model ages are younger indicating a larger mantle contribution (Fig. 10b). Further studies are necessary combining whole-rock Nd-, Pb- and Sr- and zircon Hf- and O-isotope analyses on the different types of Variscan igneous rocks to get more information on source rocks. A comparison with published and new isotopic ratios of suspected source rocks, e.g. with the Variscan mantle-derived rocks (e.g. lamprophyric dykes, Abdelfadil et al. 2013; Soder and Romer 2018) could further contribute to this discussion.

The relationship of magmatism and faulting

Igneous rocks along the northeastern boundary of the Lusatian Block resulted in ages of 312–313 Ma (biotite-bearing granites from the Koenigshain pluton, amphibole-bearing granitoids, Karkonosze pluton according to Kryza et al. 2014b). This boundary is the Intra-Lusatian Fault, which is a branch of the ISF (Fig. 2). In contrast, igneous rocks with 298–299 Ma ages (the Stolpen pluton and the volcanic rocks of the Weissig basin) prevail along the western boundary of the Lusatian Block, bound to the Lusatian Thrust Fault and the Stolpen-Klotzsche Fault which are part of the EFZ (Fig. 2b). Since there is petrologic evidence that the Variscan granitic rocks of the Lusatian Block are bound to faults (Thomas and Davidson 2016; Lisowiec et al. 2014; Mierzejewski and Oberc-Dziedzic 1990; Oberc-Dziedzic et al. 2015) and intruded within a post-collisional strike-slip environment (Edel et al. 2018; Mazur et al. 2020), these ages may give constraints for faulting activity on the EFZ and the ISF.

Tectonic activity at the EFZ has been determined previously by dating the Meissen Massif, which is bound to the EFZ and was deformed during its intrusion by dextral strike-slip movements (e.g., Hofmann et al. 2009; Linnemann et al. 2010). The rocks of the Meissen Massif, and thus the time of dextral shear, have been dated with zircon U–Pb SHRIMP (326 ± 6, 330 ± 5 Ma, Nasdala et al. 1999) and with zircon U–Pb LA–ICP–MS (334 ± 3 Ma, Hofmann et al. 2009). Ar–Ar and K–Ar ages on hornblende, biotite and muscovite revealed ages between 323.5 ± 1.0 Ma and 334.7 ± 7.0 Ma (Wenzel et al. 1997; Sharp et al. 1997). Probably, the EFZ was re-activated with different kinematics several times during the post-collisional period of the Variscan orogeny (Scheck et al. 2002; Edel et al. 2018). Our new age data of the Stolpen pluton and the volcanic rocks of the Weissig basin established a magmatic phase at 298–299 Ma that might also be linked to strike-slip deformation along the EFZ. This is within error identical to the age of the Leutewitz ignimbrite of the Meissen volcanic complex (Meissen Massif, 303 ± 3 Ma, Hoffmann et al. 2013). Consequently, two-phase tectono-magmatic activity of the EFZ can be supposed from these data.

Periods of Variscan magmatic activity in Saxothuringia

The crystallization ages of most igneous rocks of Saxothuringia have been determined by different dating methods. Extensive compilations of magmatic intrusion and eruption ages have been given e.g., by Förster and Romer (2010) and by von Seckendorff (2012). Because of its high closure temperatures, zircon U–Pb-dating is best suited to date crystallization of igneous rocks. Currently, only the high precision of CA–ID–TIMS data allows to recognize small (< 1%) differences in crystallization ages. For this reason, we compare our data with published zircon U–Pb CA–ID–TIMS data on further igneous rocks of the Saxothuringian and Tepla-Barrandian zones (Fig. 11).

This compilation of U–Pb CA–ID–TIMS data (Fig. 11) suggests the existence of two well-established magmatic episodes following the Variscan orogeny (e.g., Tischendorf and Förster 1990; Pietranik et al. 2013). Contemporaneously with the intrusion of the Koenigshain pluton and the amphibole-bearing granites of the Lusatian Block, the Karkonosze pluton (Kryza et al. 2014b), the volcanic rocks of the Tharandt Caldera of the NE Erzgebirge (Breitkreuz et al. 2021), and volcanic rocks interlayered within the Žacléř Formation of the Intra-Sudetic basin (Opluštil et al. 2016a) were formed. The intrusion of the large granite plutons of the Western Erzgebirge and of the Niederbobritzsch pluton of the NE Erzgebirge occurred slightly earlier, between 322.9 ± 0.4 Ma and 314.1 ± 0.6 Ma (Tichomirowa et al. 2019a; Breitkreuz et al. 2021). The intrusion of the Stolpen pluton and the formation of the volcano-sedimentary Weissig basin occurred simultaneously with and subsequently to the volcanic rocks of the Ilmenau Formation and preceding the deposition of the Oberhof Formation of the Thuringian Forest basin (Lützner et al. 2021). Similar, but slightly younger ages have been reported from the Chotěvice Formation of the Karkonosze piedmont basin and the Broumov Formation of the Intra-Sudetic basin (Opluštil et al. 2016a).

The Varican post-orogenic episode is characterized by polyphase strike-slip-faulting at major shear zones (Arthaud and Matte 1977; Elter et al. 2020). According to structural and microtectonic considerations, dextral faulting prevailed at the main EFZ, but at least one subordinate event of sinistral activity can be recognized at marginal faults (Mattern, 1996). From paleomagnetic, structural and geochronologic data, Edel et al. (2018) derived the timing and kinematics of several tectonic phases that affected the Variscan orogenic belt after the main collisional event. Three of these phases happened during the period of magmatic events of the Saxothuringian Zone hitherto dated with zircon U–Pb CA–ID–TIMS (Fig. 11). During a WNW–ESE extensional episode from 325 to 310 Ma, pre-existing NW striking faults were re-activated dextrally (Edel et al. 2018). These fault movements led to the abundant emplacement of granitic plutons in the Saxothuringian Zone (e.g., Linnemann et al. 2010; Edel et al. 2018) and to the less frequent occurrence of volcanic rocks within and outside of intramontane basins (Fig. 11, the Tharandt Forest Caldera and volcanic rocks in the Intrasudetic basin, Opluštil et al. 2016a). The following episode of NE–SW compression with a duration from 310 to 300 reactivated the NW striking faults sinistrally and was apparently without magmatic activity in the Saxothuringian Zone (Fig. 11, Edel et al. 2018). In contrast to the Saxothuringian data, volcano-sedimentary basins of the Tepla-Barrandean Zone do not show this gap in magmatic activity, but additionally cover the age range between 310 and 300 Ma (Opluštil et al. 2016b, Fig. 11). Finally, NNE–SSW extension from 300 to 260 Ma reactivated NW striking faults dextrally. The magmatic episode that occurred mainly at the beginning of this period, between 300 and 297 Ma (Fig. 11), is widespread in the Saxothuringian Zone. Magmatic activity mainly occurs as volcanic rocks that were deposited together with sediments in the frequent intramontane basins. The Weissig basin and the Thuringian Forest basin are two of these basins that have been biostratigraphically correlated to other Saxothuringian basins (e.g., Schneider et al. 2020). Our zircon U–Pb CA–ID–TIMS data demonstrate that this episode of volcanic activity was also accompanied by the emplacement of plutonic rocks such as the Stolpen pluton.

Conclusion

Our new zircon U–Pb CA–ID–TIMS data suggest two distinct magmatic episodes in the Lusatian Block. These two episodes took place at 312–313 Ma and 298–299 Ma. The biotite-bearing granites of Koenigshain and amphibole-bearing granites constitute the older group. The biotite-bearing granites of Stolpen and the volcanic rocks of the Weissig basin are assigned to the younger group.

New whole-rock Nd and zircon O- and Hf-isotopic data of biotite-bearing granites of the Koenigshain pluton give new insights on the sources of these rocks. The Cadomian basement of the Lusatian Block and of the Erzgebirge can be excluded as sources based on the homogeneity of zircon Hf and whole-rock Nd-isotope data and from corresponding model ages of Variscan granites. Instead, from zircon O-isotopic data, we can infer on an acid or intermediate igneous source of these I-type granites.

The new ages together with literature data suggest two temporally separate magmatic episodes probably related to faulting in the Saxothuringian Zone of the Variscan sorogen. The remarkable simultaneity of the granitoid plutons that are bound to the ISF and its branches on the one hand and of the igneous rocks that are bound to the EFZ on the other hand, suggests that the rise of magma might be linked to distinct faulting events on these shear zones. The correlation of magmatic episodes with tectonic phases of extension rather than compression (Fig. 11, Edel et al. 2018) supports this hypothesis.

Additional zircon U–Pb CA–ID–TIMS data from faulting-related Variscan post-collisional igneous rocks will help to better constrain the upper and lower age limits of these magmatic episodes. These limits would allow to reconstruct the differential tectonic setting at different times and to extend this consideration to other parts of the Variscan orogen. Further zircon and whole-rock Hf-, O-, Nd-, Sr-, Pb-isotope data for different petrological/chemical rock types and age groups will provide additional information for potential sources of these rocks.

Supplementary Information The online version contains supplementary material available at https://doi.org/10.1007/s00531-021-02092-y.

Acknowledgements The authors are grateful to Christoph Breitkreuz and Albrecht von Quadt for their very helpful and constructive reviews. We thank the Saxonian Geological Survey for financial support and the Isotope Research Centre in St. Petersburg (Russia) for SHRIMP measurements.

Funding Open Access funding enabled and organized by Projekt DEAL. This work was financed by the Saxonian Geological Survey.

Data availability All data are given in this manuscript, partly in the electronic supplement.

Declarations

Conflicts of interest None.

Code availability (software application or custom code) Not applicable.

References

Abdelfadil K, Romer RL, Seifert T, Lobst R (2013) Calc-alkaline lamprophyres from Lusatia (Germany)—evidence for a repeatedly enriched mantle source. Chem Geol 353:230–245

Arthaud F, Matte P (1977) Late Paleozoic strike-slip faulting in southern Europe and northern Africa: Result of a right-lateral shear zone between the Appalachian and the Urals. Geol Soc Am Bull 88:1305–1320

Barbarin B (2005) Mafic magmatic enclaves and mafic rocks associated with some granitoids of the central Sierra Nevada batholith, California: nature, origin, and relations with the hosts. Lithos 80:155–177

Barthel M, Eichler B, Reichel W (2010) The Lower Permian (Rotliegend) flora of the Weissig Basin. J Cent Eur Geol 56(2):159–192

Le Bas MJ, Le Maitre RW, Streckeisen A, Zanettin B, IUGS Subcommission on the Systematics of Igenous Rocks (1986) A Chemical Classification of Volcanic Rocks Based on the Total Alkali-Silica Diagram. J Petrol 27(3):745–750

Białek D, Kryza R, Oberc-Dziedzic T, Pin C (2014) Cambrian Zawidów granodiorite in the Cadomian Lusatian Massif (Central European Variscides): what do the SHRIMP zircon ages mean? J Geosci 59:313–326

Black LP, Kamo SL, Allen CM, Aleinikoff JN, Davies DW, Korsch RJ, Foudoulis C (2003) TEMORA 1: a new zircon standard for Phanerozoic U–Pb geochronology. Chem Geol 200:155–170

Black LP, Kamo SL, Allen CM, Davis DW, Aleinikoff JN, Valley JW, Mundil R, Campbell IH, Korsch RJ, Williams IS, Foudoulis C (2004) Improved $^{206}Pb/^{238}U$ microprobe geochronology by the monitoring of a trace-element –related matrix effect; SHRIMP, ID–TIMS, ELA–ICP–MS and oxygen isotope documentation for a series of zircon standards. Chem Geol 205:115–140

Bowring J. F., McLean N. M., Bowring S. A. (2011) Engineering cyber infrastructure for U–Pb geochronology: Tripoli and U–Pb_Redux, Geochem Geophys Geosys 12(6): Q0AA19

Breitkreuz C, Käßner A, Tichomirowa M, Lapp M, Huang S, Stanek K (2021) The Late Carboniferous deeply eroded Tharandt Forest Caldera-Niederbobritzsch Granite Complex: A post-Variscan long-standing magmatic system in central Europe, Int J Earth Sci, online

Cháb J, Stránik Z, Eliáš M (2007) Geological map of the Czech Republic 1: 500,000. Czech Geological Survey, Prague

Chappell BW, White AJR (2001) Two contrasting granite types: 25 years later. Aust JEarth Sci 48:489–499

Chen R-X, Zheng Y-F (2017) Metamorphic zirconology of continental subduction zones. J Asian Earth Sci 145:149–176

Condon DJ, Schoene B, McLean NM, Bowring SA, Parrish RR (2015) Metrology and traceability of U–Pb isotope dilution geochronology (EARTHTIME Tracer Calibration Part I). Geochim Cosmochim Acta 164:464–480

DePaolo DJ (1981) Neodymium isotopes in the colorado front range and crust–mantle evolution in the proterozoic. Nature 291:193–196

Duthou JL, Couturie JP, Mierzejewski MP, Pin C (1991) Next dating of granite sample from the Karkonosze Mountains using Rb–Sr total rock isochrone method. Przegla d Geologiczny 36:75–79 (in Polish, English summary)

Edel JB, Schulmann K, Lexa O, Lardeaux JM (2018) Late Palaeozoic palaeomagnetic and tectonic constraints for amalgamation of Pangea supercontinent in the European Variscan Belt. Earth-Sci Rev 177:589–612

Eidam J, Götze J (1991) The granitic massif of Königshain–Arnsdorf (Lusatian Anticlinal Zone): an example of a reversly zoned pluton. Chem Erde 51:55–71

Eidam J, Hammer J, Korich D, Bielicki K-H (1995) Characterization, distribution and genesis of amphibole-bearing variscan granites in the lusatian granodiorite Massif (Northern margin of the Bohemian Massif). Neues Jahrb Mineral Abhandlungen 168:259–281

Elter FM, Gaggero L, Mantovani F, Pandeli E, Costamagna LG (2020) The Atlas-East Variscan –Elbe shear system and its role in the formation of the pull-apart Late-Palaeozoic basins. Int J Earth Sci 109:739–760

Farina F, Stevens G, Gerdes A, Frei D (2014) Small-scale Hf isotopic variability in the Peninsula pluton (South Africa): the processes that control inheritance of source $^{176}Hf/^{177}Hf$ diversity in S-type granites. Contrib Mineral Petrol 168:1–18

Förster H-J, Romer RL (2010) Carboniferous magmatism. In: Linnemann U, Romer RL (eds) Pre-Mesozoic Geology of Saxo-Thuringia—from the cadomian active margin to the variscan orogen. Schweizerbart, Stuttgart, pp 287–308

Förster H-J, Tischendorf G, Trumbull RB, Gottesmann B (1999) Late-collisional granites in the variscan erzgebirge. Germany J Petrol 40(11):1613–1645

Förster H-J, Rhede D, Stein HJ, Romer RL, Tischendorf G (2012) Paired uraninite and molybdenite dating oft he Königshain granite: implications fort he onset of late-Variscan magmatism in the Lausitz Block. Int J Earth Sci 101:57–67

Friedl G, Finger F, Paquette J-L, von Quadt A, McNaughton NJ, Fletcher IR (2004) Pre-variscan geological events in the austrian part of the bohemian massif deduced from U–Pb zircon ages. Int J Earth Sci 93:802–823

Gerdes A, Zeh A (2006) Combined U–Pb and Hf isotope LA-(MC) ICP-MS analyses of detrital zircons: Comparison with SHRIMP and new constraints for the provenance and age of an Armorican metasediment in Central Germany. EarthPlanet Sci Lett 249:47–61

Gerstenberger H, Haase G (1997) A highly effective emitter substance for mass spectrometric Pb isotope ratio determinations. Chem Geol 136:309–312

Geyer G, Buschmann B, Elicki O (2014) A new lowermost middle Cambiran (Series 3, Stage 5) faunule from Saxony (Germany) and its bearing on the tectonostratigraphic history of the Saxo-thuringian domain. Paläontol Z 88:239–262

Hammer J (1996) Geochemie und Petrogenese der cadomischen und spätvariszischen Granitoide der Lausitz. Freib Forsch C463:1–107

Hammer J, Eidam J, Röber B, Ehling B-C (1999) Prävariscischer und variscischer granitoider Magmatismus am NE-Rand des Böhmischen Massivs–Geochemie und Petrogenese. Z Geol Wiss 27(5/6):401–415

Hecht L, Thuro K, Plinninger R, Cuney M (1999) Mineralogical and geochemical characteristics of hydrothermal alteration and episyenitization in the Königshain granites, northern Bohemian Massif, Germany. Int J Earth Sci 88:236–252

Heinonen A, Anderson T, Rämö T, Whitehouse M (2015) The source of Proterozoic anorthosite and rapakivi granite magmatism: evidence from combined in situ Hf-O isotopes of zircon in the Ahvenisto complex, southeastern Finland. J Geol Soc 172:103–112

Hintze JL, Nelson RD (1998) Violin plots: a box plot-density trace synergism. Am Stat 52(2):181–184

Hoffmann U, Breitkreuz C, Breiter K, Sergeev S, Stanek K, Tichomirowa M (2013) Carboniferous-Permian volcanic evolution in Central Europe—U/Pb ages of volcanic rocks in Saxony (Germany) and northern Bohemia (Czech Republic). Int J Earth Sci 102:73–99

Hofmann M, Linnemann U, Gerdes A, Ullrich B, Schauer M (2009) Timing of dextral strike-slip processes and basement exhumation in the Elbe Zone (Saxo-Thuringian Zone): the final pulse of the Variscan Orogeny in the Bohemian Massif constrained by LA–SF–ICP–MS U–Pb zircon data. In: Murphy JB, Keppie JD, Hynes AJ (eds.) Ancient Orogens and Modern Analogues. Geol Soc SpecPubl 327:197–214

Horstwood MSA, Košler J, Gehrels G, Jackson SE, McLean NM, Paton C, Pearson NJ, Sircombe K, Sylevester P, Vermeesch P, Bowring JF, Condon DJ, Schoene B (2016) Community-derived standards for LA–ICP–MS U-(Th-)Pb geochronology—uncertainty propagation, age interpretation and data reporting. Geostand Geoanalytical Res 40(3):311–332

Huhle K, Lange J-M (2010) Über ein vorkommen von permosiles im untergrund des schlosses wackerbarth in radebeul (Sachsen). J CentEur Geol 56(2):127–136

Jung S, Pfänder JA (2007) Source composition and melting temperatures of orogenic granitoids: constraints from CaO/Na_2O, $Al2O_3/TiO_2$ and accessory mineral saturation thermometry. Eur J Mineral 19:859–870

Kindermann A, Fiedler F, Seifert T, Uhlig S (2003) Platinmetall-Führung der Ni–Cu-Sulfidmineralisationen im Bereich der Lausitzer Antiklinalzone. Z AngewGeol 49:43–47

Kober B (1987) Single zircon evaporation combined with Pb+ emitter bedding for $^{207}Pb/^{206}Pb$-age investigations using thermal ion mass spectrometry, and implications for zirconology. Contrib Mineral Petrol 96:63–71

Kozdrój W, Krentz O, Opletal M (2001) Geological Map and Comments on the Geological Map Lausitz, Jizera, Karkonosze (without Cenozoic sediments) 1:100000. Państwowy Instytut Geologiczny, Warsaw.

Kramer W, Müller B, Peschel A (1977) Zur tektonischen und substantiellen Charakteristik der Basite des Lausitzer Antiklinoriums und deren Altersbeziehung. Z Geol Wiss 5:95–100

Kröner A, Willner AP (1998) Time of formation and peak of Variscan HP-HT metamorphism of quartz-feldspar rocks in the central Erzgebirge, Saxony, Germany. Contrib Mineral Petrol 132:1–20

Kröner A, Hegner E, Hammer J, Haase G, Bielicki K-H, Krauss M, Eidam J (1994) Geochronology and Nd-Sr systematics of Lusatian granitoids: significance for the evolution of the Variscan orogeny in east-central Europe. Geol Rdsch 83:357–376

Kroner U, Hahn T, Romer RL, Linnemann U (2007) The Variscan orogeny in the Saxo-Thuringian zone—heterogenous overprint of Cadomian/Paleozoic Peri-Gondwana crust. In Linnemann U, Nance RD, Kraft P, Zulauf G (eds.) The evolution of the Rheic

Ocean: From Avalonian-Cadomian Active Margin to Alleghenian-Variscan Collision. Geol Soc Am Spec 423:153–172
Kryza R, Schaltegger U, Oberc-Dziedzic T, Rin C, Ovtcharova M (2014a) Geochronology of a composite granitoid pluton: a high-precision ID–TIMS U–Pb zircon study of the Variscan Karkonosze Granite (SW Poland). Int J Earth Sci 103:683–696
Kryza R, Pin C, Oberc-Dziedzic T, Crowley QG, Larionov A (2014b) Deciphering the geochronology of a large granitoid pluton (Karkonosze Granite, SW Poland): an assessment of U–Pb zircon SIMS and Rb–Sr whole-rock dates relative to U–Pb zircon CA–ID–TIMS. Int Geol Rev 56(6):756–782
Kusiak MA, Dunkley DJ, Słaby E, Martin H, Budzyń B (2009) Sensitive high-resolution ion microprobe analysis of zircon reequilibrated by late magmatic fluids in a hybridized pluton. Geology 37:1063–1066
Lackey JS, Valley JW, Chen JH, Stockli DF (2008) Dynamic magma systems, crustal recycling, and alteration in the central sierra nevada batholith: the oxygen isotope record. J Petrol 49:1397–1426
Liew TC, Hofmann AW (1988) Precambrian crustal components, plutonic associations, plate environment of the Hercynian Fold Belt of central Europe: Indications from a Nd and Sr isotopic study. Contrib Mineral Petrol 98:129–138
Linnemann U, Romer RL, Gerdes A, Jeffries T, Drost K, Ulrich J (2010) The cadomian orogeny in the saxo-thuringian zone. In: Linnemann U, Romer RL (eds) Pre-mesozoic geology of saxo-thuringia: from the cadomian active margin to the variscan orogen. Schweizerbart, Stuttgart, pp 37–58
Linnemann U, Gerdes A, Hofmann M, Marko L (2014) The cadomian orogen: neoproterozoic to early cambrian crustal growth and orogenic zoning along the periphery of the west african craton—constraints from U–Pb zircon ages and Hf isotopes (Schwarzburg Antiform, Germany). Precambrian Res 244:236–278
Linnemann U, Gehmlich M, Tichomirowa M, Buschmann B, Nasdala L, Jonas P, Lützner H, Bombach K (2000) From Cadomian subduction to early Palaeozoic rifting: the evolution of Saxo-Thuringia at the margin of Gondwana in the light if single zircon geochronology and basin development (central European Variscides, Germany). In: Franke W, Oncken O, Tanner D (eds.) Orogenic Processes: Quantification and Modelling in the Variscan Belt. Geol Soc Spec Publ 179:131–153
Linnemann U (2007) Ediacaran rocks from the Cadomian basement of the Saxo-Thuringian Zone (NE Bohemian Massif, Germany): age constraints, geotectonic setting and basin development. In: Vickers-Rich P, Komarower P (eds.) The Rise and Fall of the Ediacaran Biota, Geol Soc Spec Publ 286:35–51
Lisowiec K, Budzyń B, Słaby E, Renno AD, Götze J (2013) Fluid-induced magmatic and post-magmatic zircon and monazite patterns in granitoid pluton and related rhyolitic bodies. Chem Erde 73:163–179
Lisowiec K, Budzyń B, Słaby E, Schulz B, Renno AD (2014) Th-U-total Pb timing constraints on the emplacement of the granitoid pluton of Stolpen. Germany Acta Geol Pol 64(4):457–472
Ludwig K (2000) SQUID 1.00, A User's Manual. Berkeley Geochronology Center Special Publication, Berkeley
Ludwig K (2008) Isoplot/Ex 3.70. A Geochronological Toolkit for Microsoft Excel. Berkeley Geochronology Center Special Publication No. 4., Berkeley, 76 pp
Lützner H, Tichomirowa M, Käßner A, Gaupp R (2021) Latest Carboniferous to early Permian volcano-stratigraphic evolution in Central Europe—U–Pb CA–ID–TIMS ages of volcanic rocks in the Thuringian Forest Basin (Germany). Int J Earth Sci 110:377–398
Mattern F (1996) The elbe zone at dresden—a late paleozoic pull-apart intruded shear zone. Z Dt Geol Ges 147:57–80
Mattinson JM (2005) Zircon U–Pb chemical abrasion ("CA-TIMS") method: Combined annealing and multi-step partial dissolution analysis for improved precision and accuracy of zircon ages. Chem Geol 220:47–66
Mazur S, Aleksandrowski P, Gągała Ł, Krzywiec P, Żaba J, Gaizik K, Sikora R (2020) Late Palaeozoic strike-slip tectonics versus oroclinal bending at the SW outskirts of Baltica: case of the Variscan belt's eastern end in Poland. Int J Earth Sci 109:1133–1160
McCann T (2008) The geology of central europe. volume 1: precambrian and palaeozoic, 1500 p.Mezger K, Krogstad EJ (1997) interpretation of discordant U-Pb zircon ages: an evaluation. Jmetamorph Geol 15:127–140
Mierzejewski M, Oberc-Dziedzic T (1990) The Izera-Karkonosze block and its tectonic development (Sudetes, Poland). Neues Jahrb Geol Paläontol Abh 179:197–222
Miller J, Matzel J, Miller C, Burgess S, Miller R (2007) Zircon growth and recycling during the assembly of large, composite arc plutons. J Volcanol Geotherm Res 167:282–299
Nasdala L, Wenzel T, Pidgeon RT, Kronz A (1999) Internal structures and dating of complex zircons from Meissen Massif monzonites, Saxony. Chem Geol 159:331–341
Oberc-Dziedzic T, Kryza R, Pin C (2015) Variscan granitoids related to shear zones and faults: examples from the Central Sudetes (Bohemian Massif) and the Middle Odra Fault Zone. Int J Earth Sci 104:1139–1166
Opluštil S, Schmitz M, Kachlík V, Štamberg S (2016a) Re-assessment of lithostratigraphy, biostratigraphy, and volcanic activity of the Late Paleozoic Intra-Sudetic, Krkonošze-Piedmont and Mnichovo Hradiště basins. Bull Geosci 91(2):399–432
Opluštil S, Schmitz M, Cleal CJ, Martínek K (2016b) A review of the Middle-Late Pennsylvanian west European regional substages and floral biozones, and their correlation to the Geological Time Scale based on new U-Pb ages. Earth-Sci Rev 154:301–335
Peccerillo A, Taylor SR (1976) Geochemistry of Eocene calc-alkaline volcanic rocks from the Kastamonu area, Northern Turkey. Contrib Mineral Petrol 58:63–81
Pietranik A, Storey C, Kierczak J (2013) The Niemcza diorites and monzodiorites (Sudetes, SW Poland): a record of changing geotectonic setting at ca. 340 Ma. Geol Q 57:325–334
Ratschbacher BC, Keller CB, Schoene B, Paterson SR, Anderson JL, Okaya D, Putirka K, Lippoldt R (2018) A new workflow to assess emplacement duration and melt residence time of compositionally diverse magmas emplaced in a sub-volcanic reservoir. J Petrol 59(9):1787–1809
Reichel W (2012) Rotliegend im Weißig-Becken nordöstlich von Dresden. In: Lützner H, Kowalczyk G (eds.) Stratigraphie von Deutschland X. Rotliegend. Teil I: Innervariscische Becken. Schrreihe Dt Ges Geowiss 61:633–645
Rudnick RL, Gao S (2014) Composition of the continental crust. In: Holland HD, Turekian KK (eds) Treatise on Geochemistry, Elsevier, Amsterdam, vol. 4, pp 1–51
Schaltegger U, Schmitt AK, Horstwood MSA (2015) U–Th–Pb zircon geochronology by ID–TIMS, SIMS, and laser ablation ICP–MS: Recipes, interpretations, and opportunities. Chem Geol 402:89–110
Scheck M, Bayer U, Otto V, Lamarche J, Banka D, Pharaoh T (2002) The Elbe Fault System in North Central Europe—a basement controlled zone of crustal weakness. Tectonophysics 360:281–299
Schmädicke E, Mezger K, Cosca MA, Okrusch M (1995) Variscan Sm–Nd and Ar–Ar ages of eclogite facies rocks from the Erzgebirge. Bohemian Massif, J Metamorp Geol 13(5):537–552
Schneider JW, Romer RL (2010) The late variscan molasses (Late Carboniferous to Late Permian) of the Saxo-Thuringian Zone. In: Linnemann U, Romer RL (eds) Pre-mesozoic geology of

saxo-thuringia—from the cadomian active margin to the variscan orogen. Schweizerbart, Stuttgart, pp 323–346

Schneider JW, Lucas SG, Scholze F, Voigt S, Marchetti L, Klein H, Opluštil S, Werneburg R, Golubev VK, Barrick JE, Nemyrovska T, Ronchi A, Day MO, Silantiev VV, Rößler R, Saber H, Linnemann U, Zharinova V, Shen S-Z (2020) Late Paleozoic-early mesozoic continental biostratigraphy—links to the standard global chronostratigraphic scale. Palaeoworld 29:186–238

Schneider JW, Werneburg R (2012) Biostratigraphie des Rotliegenden mit Insekten und Amphibien. In: Lützner H, Kowalczyk G (eds.) Stratigraphie von Deutschland X. Rotliegend. Teil I: Innervariscische Becken. Schrreihe Dt Ges Geowiss 61:110–142

Schoene B, Crowley JL, Condon DJ, Schmitz MD, Bowring SA (2006) Reassessing the uranium decay constants for geochronology using ID–TIMS U–Pb data. Geochim Cosmochim Acta 70:426–445

Schoene B (2014) U–Th–Pb geochronology. In: Holland HD, Turekian KK (eds) Treatise on geochemistry, Elsevier, Amsterdam, vol. 4, pp 341–378

von Seckendorff V (2012) Der Magmatismus in und zwischen den spätvariscischen permokarbonen Sedimentbecken in Deutschland. In: Lützner H, Kowalczyk G (eds.) Stratigraphie von Deutschland X. Rotliegend. Teil I: Innervariscische Becken. Schrreihe Dt Ges Geowiss 61:743–860

Sharp WD, Wenzel T, Nasdala L, Mertz DF, Becker T (1997) Geochronology of Hercynian Meissen Massif igneous rocks based on $^{40}Ar/^{39}Ar$ (amphibole, mica) and $^{206}Pb/^{238}U$ SHRIMP (zircon) data. Schrreihe Dt Geol Ges 2:108–109

Słaby E, Götze J (2004) Feldspar crystallization under magma mixing conditions evidenced by cathodoluminescence and geochemical modelling—a case study from Karkonosze pluton (SW Poland). Mineral Mag 68:541–557

Słaby E, Martin H (2005) Mechanisms of differentiation of the Karkonsoze Granite. Pol Mineral Soc Spec Papers 26:264–267

Słaby E, Martin H (2008) Mafic and Felsic Magma Interaction on Granites: the Hercynian Karkonsosze Pluton (Sudetes, Bohemian Massif). J Petrol 49(2):353–391

Sláma J, Košler J, Condon DJ, Crowley JL, Gerdes A, Hanchar JM, Horstwood MSA, Morris GA, Nasdala L, Norberg N, Schaltegger U, Schoene B, Tubrett N, Whitehouse MJ (2008) Plesovice zircon—a new natural reference material for U–Pb and Hf isotopic microanalysis. Chem Geol 249:1–35

Słodczyk E, Pietranik A, Glynn S, Wiedenbeck M, Breitkreuz C, Dhuime B (2018) Contrasting sources of Late Paleozoic rhyolite magma in the Polish Lowlands: evidence from U–Pb ages and Hf and O isotope composition in zircon. Int J Earth Sci 107:2065–2081

Soder CG, Romer RL (2018) Post-collisional potassic-ultrapotassic magmatism of the variscan orogen: implications for mantle metasomatism during continental subduction. J Petrol 59(6):1007–1034

Stacey JS, Kramers JD (1975) Approximation of terrestrial lead isotopic evolution by a two-stage model. Earth Planet Sci Lett 26:207–221

Thomas R, Davidson P (2016) Origin of miarolithic pegmatites in the Königshain granite/Lusatia. Lithos 260:225–241

Thomas R, Davidson P, Rhede D, Leh M (2009) The miarolithic pegmatites from the Königshain: a contribution to understanding the genesis of pegmatites. Contrib Mineral Petrol 157:505–523

Tichomirowa M (2002) Zircon inheritance in diatexite granodiorites and its consequence on geochronology—a case study in Lusatia and the Erzgebirge (Saxo-Thuringia, Eastern Germany). Chem Geol 191:209–224

Tichomirowa M, Berger HJ, Koch EA, Belyatski B, Götze J, Kempe U, Nasdala L, Schaltegger U (2001) Zircon ages of high-grade gneisses in the Eastern Erzgebirge (Central European Variscides)—Constraints on origin of the rocks and Precambrian to Ordovician magmatic events in the Variscan foldbelt. Lithos 56:303–332

Tichomirowa M, Whitehouse M, Nasdala L (2005) Resorption, growth, solid state recrystallization, and annealing of granulite facies zircon—a case study from the Central Erzgebirge, Bohemian Massif. Lithos 82:25–50

Tichomirowa M, Sergeev S, Berger HJ, Leonhardt D (2012) Inferring protoliths of high-grade metamorphic gneisses in the Eastern Erzgebirge using zirconology, geochemistry and comparison with lower-grade rocks from Lusatia (Saxothuringia, Germany). Contrib Mineral Petrol 164:375–396

Tichomirowa M, Whitehouse M, Gerdes A, Schulz B (2018) Zircon (Hf, O isotopes) as melt indicator: Melt infiltration and abundant new zircon growth within melt rich layers of granulite-facies lenses versus solid-state recrystallization in hosting amphibolite-facies gneisses (central Erzgebirge, Bohemian Massif). Lithos 302–303:65–85

Tichomirowa M, Käßner A, Sperner B, Lapp M, Leonhardt D, Linnemann U, Münker C, Ovtcharova M, Pfänder JA, Schaltegger U, Sergeev S, von Quadt A, Whitehouse M (2019a) Dating multiply overprinted granites: the effect of protracted magmatism and fluid flow on dating systems (zircon U–sPb: SHRIMP/SIMS, LA–ICP–MS, CA–ID–TIMS; and Rb–Sr, Ar–Ar)—Granites from the Western Erzgebirge (Bohemian Massif, Germany). Chem Geol 519:11–38

Tichomirowa M, Gerdes A, Lapp M, Leonhardt D, Whitehouse M (2019b) The chemical evolution from older (323–318 Ma) towards younger highly evolved tin granites (315–314 Ma)—sources and metal enrichment in Variscan granites of the western Erzgebigre (Central European Variscides, Germany). Minerals 9:1–30

Tischendorf G, Förster H-J (1990) Acid magmatism and related metallogenesis in the Erzgebirge. Geol J 25:443–454

Valley JW, Lackey JS, Cavosie AJ, Clechenko CC, Spicuzza MJ, Basei MAS, Bindeman IN, Ferreira VP, Sial AN, King EM, Peck WH, Sinha AK, Wei CS (2005) 4.4 billion years of crustal maturation: oxygen isotope ratiosof magmatic zircon. Contrib Mineral Petrol 150:56–580

Vellmer C, Wedepohl KH (1994) Geochemical characterization and origin of granitoids from the South Bohemian Batholith in Lower Austria. Contrib Miner Petrol 188:13–32

von Quadt A, Wotzlaw J-F, Buret Y, Large SJE, Peytcheva I, Trinquier A (2016) High-precision zircon U/Pb geochronology by ID-TIMS using new 10^{13} ohm resistors. J Anal at Spectrom 31:658–665

Watson EB, Harrison TM (1983) Zircon saturation revisited: temperature and composition effects in a variety of crustal magma types. Earth Planet Sci Lett 64:295–304

Wenzel T, Mertz DF, Oberhänsli R, Becker T, Renne PR (1997) Age, geodynamic setting, and mantle enrichment processes of a K-rich intrusion from the Meissen massif (northern Bohemian massif) and implications for related occurrences from the mid-European Hercynian. Geol Rundsch 86:556–570

Widmann P, Davies JHFL, Schaltegger U (2019) Calibrating chemical abrasion: its effects on zircon crystal structure, chemical composition and U–Pb age. Chem Geol 511:1–10

Wiedenbeck M, Alle P, Corfu F, Griffin WL, Meier M, Oberli F, von Quadt A, Roddick JC, Spiegel W (1995) Three natural zircon standards for U–Th–Pb, Lu–Hf, trace element and REE analysis. Geostand Newsl 19(1):1–23

Wiedenbeck M, Hanchar J, Peck WH, Sylvester P, Valley J, Whitehouse M, Kronz A, Morishita Y, Nasdala L (2004) Further characterisation of the 91500 zircon crystal. Geostand Geoanal Res 28(1):9–39

Williams IS (1998) U-Th-Pb geochronology by ion microprobe. In: McKibben MA, Shanks WC, Ridley WI (eds.) Applications of Microanalytical Techniques to Understanding Mineralizing Processes. Rev Econ Geol 7:1–35

Zieger J, Linnemann U, Hofmann M, Gärtner A, Marko L, Gerdes A (2018) A new U–Pb LA–ICP–MS age of the Rumburk granite (Lausitz Block, Saxo-Thuringian Zone): constraints for a magmatic event in the Upper Cambrian. Int J Earth Sci 107:933–953